# A network of coiled-coil and actin-like proteins controls the cellular organization of magnetosome organelles in deep-branching magnetotactic bacteria

Virginia V. Russell[1], Anthony T. Iavarone[2], Ertan Ozyamak[1,3], Carly Grant[1,4] and Arash Komeili[1]

[1] Plant and Microbiology, University of California Berkeley, Berkeley, California, USA.
[2] QB3/Chemistry Mass Spectrometry Facility, University of California Berkeley, Berkeley, California, USA.
[3] Current affiliation: Bio-Rad Laboratories, Hercules, California, USA
[4] Current affiliation: Entrepreneurship Program, UCSF Rosenman Institute, San Francisco, California, USA

## Abstract

Magnetotactic Bacteria (MTB) are a diverse group of microorganisms that use magnetosomes, organelles composed of magnetite or greigite, to navigate along geomagnetic fields. While MTB span several phyla and exhibit diverse phenotypes, magnetosome formation has been mechanistically studied in only two species of *Alphaproteobacteria*. Here, we use *Desulfovibrio magneticus* RS-1 to uncover the mechanisms behind tooth-shaped magnetosome assembly in deep-branching MTB. Our findings reveal that RS-1 magnetic particles initially form randomly within the cell before localizing to the positive cell curvature. Genetic and proteomic analyses indicate that early biomineralization involves membrane-associated proteins found in all MTB, while later stages depend on coiled-coil (Mad20, 23, 25, and 26) and actin-like (MamK and Mad28) proteins, most of which are unique to deep-branching MTB. These findings suggest that while biomineralization originates from a common ancestor, magnetosome chain formation has diverged evolutionarily among different MTB lineages.

## Introduction

Magnetotactic Bacteria (MTB) are a diverse group of microorganisms that navigate along geomagnetic fields to locate low-oxygen environments in a process termed magneto-aerotaxis. This ability relies on magnetosomes—specialized organelles containing magnetic crystals of magnetite ($Fe_3O_4$) or greigite ($Fe_3S_4$) 50-70 nm in diameter, enclosed by a lipid bilayer membrane with unique set of proteins[1,2]. Depending on the species, magnetosomes form single or multiple chains, that allow for alignment with external fields[3]. These features have made MTB models for studying bacterial organelle formation, biomineralization, and the global geochemical cycling of iron[4]. MTB have also been deployed as potential vehicles for a variety of biotechnological applications[5]. A key bottleneck in the study of MTB has been the limited number of model organisms that sufficiently represent the mechanistic diversity and evolution of magnetosome formation.

MTB are a polyphyletic group of microorganisms that belong to *Alphaproteobacteria*, *Gammaproteobacteria*, *Candidatus Etaproteobacteria* classes in the *Pseudomonadota* phylum, and the phyla *Desulfobacterota*, *Nitrospirota, Candidatus Omnitrophota*, and *Elusimicrobiota* (Figure 1B). Metagenomic studies suggest MTB may also exist in the *Latescibacteria*, *Planctomycetes*, *Nitrospinota*, *Fibrobacterota*, *Riflebacteria*, *Hydrpgendentota*, *Myxococcota*, *Bdellovibrionota* phyla and possibly more[2,6]. MTB exhibit diverse phenotypes, including variations in crystal shape, chain organization, and magnetosome composition[3]. Phylogeny correlates with some of these features; for instance, *Alphaproteobacteria* produce cubooctahedral and prismatic magnetite crystals, while *Desulfobacterota* and other deep-branching MTB (*Nitrospirota*, *Omnitrophota*, *Elusimicrobiota*) form irregular tooth-shaped magnetite crystals thought to represent the ancestral magnetosome form[3](Figure 1C).

Despite the vast diversity of MTB, most mechanistic studies have focused on two Alphaproteobacterial species, *Magnetospirillum magneticum* AMB-1 and *Magnetospirillum gryphiswaldense* MSR-1, which contain a conserved magnetosome gene cluster (MGC). The MGC spans ~100 kilobases and includes 50-100 genes, with 29 necessary and sufficient for magnetosome formation[7]. Among these, only five core genes (*mamA*, *B*, *I*, *E*, and *Q*) are shared across all MTB[8,9]. Many genes critical for magnetosome formation in *Alphaproteobacteria* are absent in other MTB. Other sets of conserved genes, called *mad* (**ma**gnetosome **d**eep branching) are found in all deep-branching MTB, *man* (**ma**gnetosome **n**itrospirota) genes are found in *Nitrospirota*, and *mae* (**ma**gnetosome **e**lusimicrobiota) genes are found in *Elusimicrobiota*[8]. However, few non-*Alphaproteobacterial* MTB are cultured, and most lack genetic systems, limiting insights into *mad* gene function and irregular tooth-shaped magnetosome formation. This is a critical barrier in the study of MTB as tooth-shaped magnetosomes are common in nature[3], yet their biomineralization mechanisms remain unknown.

The most promising model for deep-branching MTB is *Desulfovibrio magneticus* RS-1, a sulfate-reducing obligate anaerobe from the *Desulfobacterota* phylum[10,11]. RS-1 synthesizes a single chain of irregular tooth-shaped magnetite magnetosomes, organized into subchains of contiguous crystals separated by gaps along the positive cell curvature (Supplemental Figure S4E, Figure 2D-*ii*). It is one of the few cultured non-Alphaproteobacterial MTB with a sequenced genome and the only deep-branching strain with tools for heterologous gene expression and genome editing[12–14]. Previous studies of RS-1 have highlighted several features distinguishing it from *Alphaproteobacterial* models. First, RS-1 produces tooth-shaped crystals. Second, unlike *Alphaproteobacteria*, mature RS-1 crystals appear to lack a lipid membrane[15], though its MGC contains transmembrane domain proteins. Genetic studies show mutations in these genes disrupt magnetite formation, implying the involvement of a magnetosome membrane at some stage[12]. Finally, RS-1, like all deep-branching MTB, contains a suite of *mad* genes, most of which do not have known functions.

Here, we comprehensively characterize the RS-1 biomineralization process using proteomics and genetics to define new pathways of magnetosome formation unique to deep-branching MTB. Using a conditional biomineralization assay combined with genetics and proteomics, we define specific steps in magnetic particle growth and identify specific factors associated with the progression of biomineralization and magnetosome chain formation. We find that early steps of biomineralization utilize proteins enriched in transmembrane domains including some encoded by *mam* genes common to all MTB. In contrast, localization, organization and positioning of the magnetosome chain rely on a suite of coiled-coil domain-containing Mad proteins as well as the actin-like proteins, MamK and Mad28. These findings indicate a complex evolutionary history where iron biomineralization is ancestral feature of all MTB while chain formation follows a divergent group-specific path.

## Results

### Hydrogen inhibition of magnetosome synthesis

Our first goal was to develop a robust system to visualize the steps of magnetosome formation in RS-1. In other MTB, magnetite is not formed under iron-limiting conditions. Addition of iron then triggers synchronized magnetosome chain development[16]. However, transitioning from iron-limited to iron-replete conditions in RS-1 leads to the accumulation of ferrosomes[15] — organelles involved in storage and detoxification of iron[17,18]. The abundance and appearance of ferrosomes in electron microscopy obscure magnetosomes, making it impossible to visualize the early stages of magnetite biomineralization. To overcome this limitation, we sought an alternative method of magnetosome inhibition that avoids iron starvation.

Serendipitously, we discovered that growth in hydrogen instead of nitrogen headspace significantly reduces RS-1's magnetic response (measured as the coefficient of magnetism ($C_{Mag}$)[19]) (Figure 2A). A trace magnetic response at high hydrogen concentrations suggested the need for hydrogen exposure throughout the culture medium. To test this, we flushed both the headspace and medium with 5% hydrogen and grew cells while spinning. Under these conditions, cultures showed no magnetic response as indicated by a $C_{Mag}$ of 1 (Figure 2C), and absence of magnetosomes when viewed by transmission electron microscopy (TEM) (Figure 2D).

One explanation for these observations is that hydrogen inhibits RS-1 growth, indirectly preventing magnetosome formation. However, growth measurements showed similar final cell densities in hydrogen and nitrogen (Figure 2B), with hydrogen-grown cells doubling faster (6 vs. 8 hours) (Figure 2B). Another possibility is that hydrogen limits iron uptake, restricting magnetosome production. To test this, we used the post-iron-starvation accumulation of ferrosomes as a proxy for iron uptake. Cells were grown in hydrogen and iron-limiting conditions and subsequently exposed to iron with either a nitrogen or hydrogen headspace. Ferrosomes were formed in both nitrogen and hydrogen (Figure 2E *iii* and *iv*), but magnetosomes formed only in nitrogen conditions (Figure 2E-*iv*). This indicates hydrogen does not inhibit iron uptake. Finally, abundance of magnetosome proteins does not change significantly at a global level (Extended Results).

## Characteristics of early and late stages of biomineralization

We next hypothesized that switching from hydrogen to nitrogen conditions under iron replete conditions could restore magnetosome formation without ferrosome interference. To test this, RS-1 was grown with 10% hydrogen to eliminate magnetosomes, then transferred to nitrogen infused medium. As predicted, magnetic response increased over time (Figure 2F), no ferrosomes were formed, and only magnetosomes were observed (Figure 2G *i*-*iii*). This transition provides a reliable method to synchronize magnetosome formation and study biomineralization.

To capture early stages of biomineralization, RS-1 was incubated shaking in hydrogen-infused medium for several passages to eliminate existing magnetosomes (Figure 2D-*i*). Cells were then transferred to nitrogen-infused medium and harvested once a measurable magnetic response ($C_{Mag}$ 1.05-1.15) was detected. Early timepoints in biomineralization showed an average of 3 magnetosomes per cell (Figure 3A, 3C). Many cells contained both mature and immature crystals (Figure 3A-*ii*). The median crystal length was 38 nm, with a bimodal distribution indicating both immature and mature crystals present (Figure 3D). Similarly, the shape factor (width-to-length ratio) followed a bimodal pattern, with peaks around 1 for immature and 2 for mature crystals (Figure 3E). During the late stages of biomineralization ($C_{Mag}$

1.3-1.5), cells contained complete magnetosome chains composed of smaller subchains (Figure 3B), averaging 12 crystals per cell (Figure 3C), all localized to the positive cell curvature. The average crystal length was 51 nm with a shape factor of 1.7, both fitting a normal distribution due to presence of fewer immature crystals (Figure 3D, 3E). These findings point to a crystal growth pattern similar to that proposed for other deep-branching MTB[20]. RS-1 crystals nucleate and grow equidimensionally to approximately 30 nm before elongating anisotropically at one end to produce a tooth-shaped morphology (Figure 3G). High-magnification TEM images revealed two mature magnetosome morphologies: curved and straight (Figure 3F *ix* and *x*). Perhaps, during elongation, crystals develop into either a straight or curved form (Figure 3F-*v*, 3F-*vi*).

While observing biomineralization stages, we discovered that subcellular magnetosome location correlates with crystal maturation. In early stages, nearly all mature crystals are positioned at the positive cell curvature, where magnetosome chains typically form, but only about 25% of immature crystals are located there (Figure 3H, 3I). In contrast, *Alphaproteobacterial* MTB such as AMB-1 and MSR-1, localize magnetosome membranes to the positive curvature before biomineralization begins[2,21].

## Distinct proteomes differentiate early- and late-stage magnetosomes

We next investigated if specific cohorts of proteins were associated with distinct biomineralization stages. Cells from early and late stages were harvested and lysed, and magnetosomes were isolated using a magnetic column. Proteomic analysis of cell lysates and magnetosome fractions via liquid chromatography-mass spectrometry focused on RS-1 MGC-encoded proteins enriched at each stage. Early-stage magnetosomes were enriched for Mad10, MamB, MamA, Mad4, FmpA, FmpB, and MamEO-Cter (Figure 3J), many of which contain predicted transmembrane domains. Late-stage magnetosomes were enriched for Mad20, Mad23, Mad28, and MamK, all of which lack transmembrane domains (Supplemental Figure 3A). The actin-like domains in Mad28 and MamK (Supplemental Figure 3A) suggest roles in chain alignment and organization. These results reveal a shift in membrane association and chain organization from early to late stages.

## Early magnetosome proteins regulate biomineralization activity

We next turned to genetics to provide functional evidence for stage-specific action of magnetosome proteins. Previous studies using chemical and UV mutagenesis identified RS-1 mutants with severe biomineralization defects, including several alleles of *mamB* that lack a magnetic response and do not produce crystals[12]. This phenotype corroborates our finding that MamB preferentially associates with early-stage magnetosomes (Figure 3J).

In contrast to *mamB*, mutants in *fmpA* and *fmpB* can still produce some magnetic particles[12]. Both FmpA and FmpB contain transmembrane domains and serine protease/denitrogenase Fe-Mo domains and are enriched on magnetosomes at the early stages of biomineralization (Supplemental Figure 3A and Figure 3J). Detailed TEM analysis revealed distinct defects for each strain: *fmpA* mutants produce misshaped circular or symmetrical crystals (Figure 4A, G), while *fmpB* mutants form smaller WT-like crystals, some of which are misshaped (Figure 4B, H). Consistent with previous findings[12], both mutants exhibit significantly fewer crystals per cell, smaller crystal sizes, and a reduced shape factors as compared to WT (Figure 4D, 4E, and 4F).

In addition to the defects in crystal shape and size, *fmpA* and *fmpB* mutants exhibited abnormal crystal placement with most crystals not localized to the cell's positive curvature (Figure 4J). The crystals of the *fmpA* mutant also fail to form chains, while only 5% of *fmpB* mutant cells show chain organization (Figure 4I). These findings suggest FmpA and FmpB are crucial for early magnetosome synthesis and indicate that biomineralization likely initiates away from the positive curvature. We propose that crystal nucleation occurs throughout the cell and crystals are later transported to the positive curvature post-maturation. Without FmpA and FmpB, crystals could remain "stuck" at nucleation sites, blocking their relocation and preventing new crystal formation, resulting in fewer crystals in mutant cells (Figure 4D).

### Initiation of chain formation by Mad10

Mad10 is more abundant in early-stage magnetosome samples than in late stages and has the highest abundance ratio among MGC proteins at the magnetosome compared to the cell lysate under all conditions (Supplemental Figure 8A). Previous studies identified Mad10 as a magnetite-binding protein[22,23] and hypothesized a role in magnetite nucleation or shape control. To investigate its function, we deleted *mad10* in RS-1 via allelic exchange. The Δ*mad10* mutant shows a significantly reduced magnetic response, which is restored by plasmid-based *mad10* expression (Supplemental Figure 1B, 1C). Despite the low Cmag, however, crystal size and shape remain unchanged and, instead, magnetosomes cluster in a single location within the cell (Figure 5A, Supplemental Figure 1I). Crystal numbers also vary widely per cell (Supplemental Figure 1D), likely due to unequal distribution during cell division. These findings indicate that Mad10 is essential for magnetosome chain organization but not for crystal size or shape regulation (Figure 5A).

## A module of Mad proteins assembles the magnetosome subchain

We next targeted genes encoding proteins more abundant in late stages of biomineralization (Figure 3J) and neighboring genes potentially belonging to the same operon (Figure 1A). All deletions were successfully complemented via plasmid-based expression (Supplemental Figures 1C, 6A-G). Mutants exhibited a range of defects which were quantified based on chain placement, magnetosome distribution, and chain/subchain phenotypes (Supplemental Figure 7F-I).

This analysis identified Mad20, Mad23, Mad25, and Mad26 as a module for magnetosome subchain assembly in RS-1. In the Δ*mad23* mutant, single magnetosomes are dispersed, with the fewest crystals per subchain among mutants and WT (Figure 5C, Supplemental Figure 1E, 6J). The strain also has the lowest $C_{Mag}$ of all chain organization mutants (Supplemental Figure 1B), suggesting Mad23 connects individual magnetosomes to form subchains. In contrast, the Δ*mad20* mutant forms distinct subchains, some linear, and others in the form of rings, clusters, or curved lines (Figure 5B). It has fewer subchains than WT (Supplemental Figure 1F, 6I), but each contains more magnetosomes (Supplemental Figure 1E). This suggests Mad20 regulates crystal influx into subchains; without it, excess crystals cause curling and distortion (Supplemental Figure 6I). Δ*mad25* and Δ*mad26* mutants show similar phenotypes (Figure 5D-E), with subchain and crystal numbers comparable to WT (Supplemental Figure 1F, D). However, most subchains cluster or form rings, especially in Δ*mad26*, where ~80% cluster and 15% form rings (Supplemental Figure 7E). These findings indicate Mad25 and Mad26 are essential for maintaining subchain linearity.

Overall, these mutants reveal an RS-1 magnetosome chain organization distinct from *Alphaproteobacterial* MTB. In AMB-1, for example, TEM shows subchains of magnetic particles, separated by empty magnetosome membranes all of which are organized into a continuous chain[24]. In contrast to AMB-1, some RS-1 mutants exhibit clusters, rings, or curved subchains within the same cell, suggesting subchains are a fundamental structural unit of chain architecture in RS-1.

## MamK and Mad28 control subchain separation and chain localization

Mad28 and MamK were selected for genetic analysis due to their higher abundance in late-stage magnetosomes (Figure 3J) and their actin-like domains (Supplemental Figures S3A and S5). *mamK* is present in nearly all MTB and is well-studied in AMB-1 and MSR-1[21,25,26]. In AMB-1, *mamK* deletion disrupts chain cohesion[21], creating gaps that affect equal distribution during cell division[27]. In MSR-1, *mamK* deletion results in mislocalized chains, mostly away from the mid-cell[28]. Similarly, in RS-1, we find that MamK plays a role in chain organization. Deletion of *mamK* eliminated the subchain phenotype (Figure 5G, Supplemental Figure 1F), leading to a single continuous chain, which sometimes wrapped around itself, resembling multiple chains. These mutants also had more crystals per cell compared to WT (Figure 5N, Supplemental Figure 1D).

RS-1, contains another magnetosome gene with an actin-like domain, *mad28*[9,29](Supplemental Figure 3A), found in all deep-branching MTB and previously suggested to have a similar role to MamK [29]. Surprisingly, deleting *mad28* in RS-1 resulted in a phenotype distinct from that of the Δ*mamK*. In Δ*mad28*, WT-like subchain organization was retained. However, chains were no longer exclusively localized to the positive cell curvature and were found pole-to-pole at mid-cell, as well as organized diagonally or transversely across the cell (Figure 5F, 5J, 5K).

To further distinguish between the Δ*mad28* and Δ*mamK* strains, we examined chain formation in a biomineralization time-course experiment. In Δ*mad28*, chain assembly followed the WT pattern, with a single mature crystal forming first, followed by subchain development and crystal incorporation (Figure 5I-K). However, chains were mispositioned from the start, forming pole-to-pole or diagonal/transverse orientations instead of localizing to the positive curvature as in WT (Figure 5J-K). In contrast, Δ*mamK* exhibited a distinct chain formation pattern. Early biomineralization resembled WT, but as crystals matured, subchains failed to develop, resulting in a single continuous chain (Figure 5L). Δ*mamK* mutants also had more magnetosomes per cell and a higher $C_{Mag}$ than WT at both biomineralization stages (Figure 5N, 5M, Supplemental Figure 1B), a phenotype not observed in other *mamK* mutants[21,28]. These findings suggest that Mad28 aligns magnetosomes to the positive curvature early in chain formation, while MamK distributes subchains along the cell length, ensuring proper alignment and potentially regulating magnetosome production.

## Interaction Network of chain organization proteins

Bioinformatic analysis shows that Mad10, 20, 23, 25, and 26 contain coiled-coil domains which can facilitate a variety of protein-protein interactions[30] (Supplemental Figure 3A). Mad23 also has HEAT repeat domains, known for similar functions. Additionally, MamK and Mad28 can form homo- and heteropolymers[29]. Thus, we hypothesized that these chain formation proteins may interact with one another. To explore potential interactions, we conducted Bacterial Adenylate Cyclase Two-Hybrid (BACTH) assays[31] (Supplemental Figure 2). We created N- and

C-terminal fusions to T25 and T18 domains for each protein and tested all interaction combinations (Supplemental Figure 9). Interactions were classified based on color intensity: dark blue spots as strong (+++), medium blue as moderate (++), and light blue as minor (+) (Supplemental Figure 2B). Our results reveal an extensive and complex network of potential interactions. All proteins exhibited self-interactions in at least one fusion combination. Mad25 interacted with all tested proteins, while Mad20, 23, 26, and MamK interacted with three or more. Mad10, interacted with itself, Mad23, and Mad25. Mad28 interacted only with Mad25 (Supplemental Figure 2A-D). These findings provide further evidence for the existence of a distinct chain organization pathway in deep-branching MTB, dependent on the interactions of coiled-coil and actin-like proteins.

## Discussion

In this study, we used a new workflow to track biomineralization in *Desulfovibrio magneticus* RS-1, a representative of deep-branching MTB, to describe an organelle assembly process distinct from *Alphaproteobacterial* species. Our work suggests a new model of magnetosomes formation with the following steps (Figure 6):

**Step 1: Nucleation and Growth.** Biomineralization initiates at randomly distributed membrane-bounded nucleation sites that are likely membrane-enclosed. Mutations in *fmpA* and *fmpB* impair crystal maturation, reduce crystal numbers, and disrupt localization to the positive curvature, linking biomineralization to chain formation. **Step 2: Crystal Maturation and Localization.** As crystals mature, they are transported to the cell’s positive curvature. Based on findings here and in previous work, we suggest that at some stage during biomineralization magnetite crystals are released from the membrane. Mad10, previously shown to interact with magnetite[22], may facilitate this transition. Bacterial two-hybrid results suggest an assembly pathway where Mad10 interacts with Mad23, which subsequently connects to Mad25. **Step 3: Subchain Assembly.** Initially, one or two mature crystals appear at the positive curvature. Mad23 links accumulating crystals to form subchains, which may be stabilized by Mad25 and Mad26. **Step 4: Chain Elongation and Positioning.** In parallel to the previous steps, subchains are distributed along the cell length by MamK, while Mad28 ensures their localization to the positive curvature. MamK's role in chain organization is conserved across MTB, as RS-1 MamK can partly complement *mamK* loss in MSR-1[29]. However, RS-1 MamK has unique functions, as its absence results in the loss of subchains and the formation of longer chains with more crystals per cell. Interestingly, Mad28 from deep-branching MTB partially complements

MamK loss in MSR-1[29], but our findings suggest Mad28 primarily localizes the chain, while MamK organizes it.

This model reveals several key differences between RS-1 and other established model organisms. First, biomineralization in RS-1 occurs one or a few crystals at a time and is a prerequisite step for chain formation, whereas in Alphaproteobacterial MTB, magnetosome membranes form chains independently of biomineralization[32]. Second, RS-1 magnetosomes have a dynamic proteome that changes with biomineralization stages, while, with a few exceptions, AMB-1 and MSR-1 maintain a largely constant proteome[2,33,34]. Finally, RS-1 and Alphaproteobacterial MTB use different sets of proteins for chain formation. The domain architecture of their respective magnetosome proteins provide further evidence for the unique features of each MTB group. For instance, 67% of AMB-1 magnetosome proteins, but only 38% RS-1's, are predicted to contain transmembrane domains (Supplemental Figure 4A-B). However, nearly ~24% (10 proteins) of RS-1 magnetosome proteins contain predicted coiled-coil domains, in contrast to ~6% (3 proteins) of AMB-1's magnetosome proteins (Supplemental Figure 4C-D). Additionally, other than MamK, all known magnetosome chain formation factors of AMB-1 and MSR-1 (MamJ, MamY, LimJ, MamK-like, McaA, and McaB) are absent in RS-1. Similarly, MTB of the deep-branching *Elusimicrobiota* phylum which do not form organized magnetosome chains are missing MamK as well as the chain formation Mad proteins. Therefore, we suggest that these coiled-coil proteins, which may organize into intermediate filaments similar to other bacterial proteins, along with the actin-like MamK and Mad28, represent a mode of chain organization unique to deep-branching MTB.

Collectively, our findings shed further light on the evolution and diversification of magnetosomes. Nearly all MTB share genes involved in membrane formation (*mamQ*), iron transport (*mamB*), and chain organization (*mamK*), likely forming the foundations of an ancient iron-accumulating organelle. Diverse magnetosome phenotypes, such as crystal shape variations, may have emerged through addition of subgroup-specific proteins to this core system. In our model, RS-1 and other deep-branching MTB evolved to organize biominerals into chains using Mad proteins, while Alphaproteobacterial MTB developed a system to align magnetosome membranes into chains using Mam proteins. This evolutionarily distinct solution may have arisen to combat the previously described conflict between magnetocrystalline orientation of tooth-shaped magnetosomes and their function as a navigational tool[35,36].

## Methods

### Multiple-sequence alignments and tree construction

Dataset was designed by searching IMG/M ER[37] for all known MTB species with homologs for all five of the core *mam* genes selected: *mamK*, *mamA*, *mamB*, *mamM* and *mamQ*. Next, the dataset was refined to encompass only species with available genomes and accessible TEM images, enabling the identification of magnetosome gene sets (*mam*, *mms*, *mad*, *man* and *mae*) for each species, along with their respective crystal shapes and compositions. Supplemental table 1 is a list of all species included in designing the phylogenetic tree for this analysis. Once the dataset was complete, the 16S DNA sequences for each species were obtained from NCBI or IMG-M [37] (Supplemental table 1). Sequences were aligned using MAFFT version 7.490 using the scoring matrix 1PAM/ k=2 [38]. Next, the aligned sequences were used to generate the maximum likelihood tree using PhyMLTree version 3.3.20180621 using GTR substitution model with 1000 bootstraps [39]. Additionally, the tree was rooted with *Omnitrophus magneticus* SKK-01.

### General Culturing for RS-1

*Desulfovibrio magneticus* RS-1 strains were grown at 30°C anaerobically in RS-1 growth medium (RGM), as described previously [12,15]. For growth with hydrogen, the medium was gassed with 10% hydrogen balanced with Nitrogen prior to autoclaving the medium. Additionally, after inoculating, the headspace was re-gassed with the same concentration of hydrogen/nitrogen gas mixture for 10 minutes. All hydrogen cultures were grown spinning on a wheel in the 30°C incubator. Cultures with nitrogen in the headspace that were used as controls for these hydrogen cultures were grown on a wheel in the incubator. All other nitrogen cultures were grown without shaking.

For experiments with different concentrations of hydrogen (Figure 2A), RS-1 WT strain was grown at 30°C anaerobically in RS-1 growth medium (RGM), as described above. Initially, all culture tubes were purged with nitrogen gas. Subsequently, prior to inoculation, varying volumes of nitrogen from the headspace were displaced and substituted with an equivalent volume of 100% hydrogen gas, aiming to achieve distinct concentrations of hydrogen in the headspace. Afterwards, RS-1 was inoculated into the culture tubes. Optical density and magnetic response via $C_{mag}$ was monitored throughout growth as previously described [12].

### Culturing for proteomics

Cultures for hydrogen vs. nitrogen consisted of 350 mL cultures with 2/3 volume of headspace, which were prepared by gassing either with nitrogen or 10% hydrogen and grown by shaking at room temperature. At late exponential phase, cultures were harvested by centrifugation at 8,000 rpm using the Beckman Model J2-21M/E centrifuge. Cell pellets were stored at -80°C until lysis and preparation for proteomic analysis. To examine different stages of biomineralization, 300 mL initial cultures were grown with hydrogen in the headspace to remove all magnetosomes. $C_{mag}$ was measured as described previously[12] and TEM images were taken of initial cultures to ensure no magnetosomes were present. Then 10 1L bottles of RGM-X medium were prepared by infusing the medium with nitrogen and gassing the headspace with nitrogen. Each of the 3 biological replicates consisted of 10 1L bottles, which were inoculated with the same starting culture. Three bottles were used for late biomineralization, which were inoculated with 10 mL of starting culture, and seven bottles were used for early biomineralization samples, which were inoculated with 20 mL of the starting culture. The cultures were grown in a 30°C incubator and OD and $C_{mag}$ were taken 2X daily. When cultures reached a $C_{mag}$ of 1.05-1.15 seven of the bottles were harvested for early biomineralization samples by centrifugation at 8,000 RPM. Subsequently, when the final 3 bottles had a $C_{mag}$ between 1.30-1.5 they were harvested for late stages of biomineralization samples also by centrifugation at 8,000 RPM. Cell pellets were stored at -80°C until it was time to prepare samples for proteomics. Each biological replicate originated from a single colony, which was inoculated into 200 mL pre-culture bottles grown with hydrogen. Each 200 mL pre-culture was subsequently used to inoculate a set of ten 1L bottles, resulting in three 10L cultures derived from three separate colonies.

### Collecting proteins associated with magnetosomes using a magnetic column

After harvesting cultures, cell pellets were resuspended in buffer A (25 mM Tris, pH 7.0, 100 mM sucrose, 1 µg/mL Leupeptin, 1 µg/mL Pepstatin A, and 1 mM PMSF. Cells were lysed three times at 25 kpi using the Single Shot feature of the Multi Cycle (MC) Cell Disruptor from Constant Systems[40]. Magnetic LS Columns (130-042-401) from Miltenyi Biotec were used to separate the magnetosomes from the cell lysate. Magnetic columns were primed with a wash with buffer A, followed by the attachment of magnets to the outside of the columns. Subsequently, the cell lysate was passed through the column by gravity flow. Flow through fractions were passed over the column two more times and buffer A was used for three additional washes. Following wash cycles, the magnets were detached from the column, and 500 µL of buffer A was pipetted into the column. The plunger provided with the column was then to provide additional force to collect all of the magnetosomes. Some of the cell lysate from each sample was also saved as a control. Next, a Bradford assay was conducted on all samples to determine the protein concentration, and if necessary, samples were concentrated during this stage. Finally, all samples were trypsin-digested as previously described[17] to prepare them for liquid chromatography-mass spectrometry, as detailed below.

## Liquid chromatography-mass spectrometry

Trypsin-digested protein samples were each analysed in triplicate using an Acquity M-class ultra-performance liquid chromatography (UPLC) system that was connected in line with a Synapt G2-Si mass spectrometer (Waters, Milford, MA) as described elsewhere[17]. Data acquisition and analysis were performed using MassLynx (version 4.1, Waters) and Progenesis QI for Proteomics software (version 4.2, Waters Nonlinear Dynamics). Data were searched against the *Desulfovibrio magneticus* strain RS-1 translated protein database to identify peptides[41].

## Plasmid and cloning and deletion

All plasmids used in this study for generating deletions and for their complementations in RS-1, as well as for plasmids used in the BACTH assays, are listed in Supplemental table 3. In-frame deletion vectors targeting *mad10*, *mad20*, *mad23*, *mad25*, *mad26, mad28* and *mamK* were constructed by amplifying upstream and downstream homology regions of RS-1 genomic DNA, using the primers listed in Supplementary Table 3. The homology regions were then inserted into the XbaI site of pAK1127 using the Gibson cloning method. The P*npt* -*strAB* cassette was subsequently inserted between the upstream and downstream homology regions of the deletion vector. Plasmids were transformed into E. coli WM3064 and then transferred to *D. magneticus* RS-1 using conjugation methods as described previously [13]. Allelic replacement of *mad10, mad20, mad23, mad25, mad26, mad28* or *mamK* with *strAB* was achieved with streptomycin selection and using two counterselections, 5-Flurouracil and sucrose. All deletions were confirmed by PCR followed by full genomic Illumina sequencing using SeqCenter (https://www.seqcenter.com).

To generate plasmids used to complement deletion strains, the genes *mad10*, *mad20*, *mad23*, *mad25*, *mad26, mad28* and *mamK* were individually amplified using primers listed in Supplemental table 4 and were cloned into pAK906 (containing the *npt* promoter) and pAK907 (containing a *mamA* promoter) using Gibson assembly. Both complementation plasmids for each gene were tested by transformation into the respective RS-1 deletion strain. Each strain, containing different versions of the complementation plasmid, was grown in liquid culture and evaluated by $C_{mag}$ measurements and TEM to determine which provided the best complementation. The plasmid that most effectively restored the phenotype was selected for further experiments.

To generate plasmids used in the BACTH studies, *mad10, mad20, mad23, mad25, mad26, mad28* and *mamK* were either synthesized by Twist Bioscience (https://www.twistbioscience.com) or PCR amplified using the primers listed in Supplementary Table 4 and were cloned into pKT25 or pKNT25 (the N or the C-termini of the T25 fragment) and pUT18 or pUT18C (the N or the C-termini of the T18 fragment) vectors in frame with the T25 and T18 fragment open reading frames by Gibson assembly.

### Biomineralization time course using hydrogen

RS-1 strains were grown at 30°C anaerobically, as described above. Initial cultures were all grown with medium infused with 10% hydrogen and headspace was purged again with 10% hydrogen after inoculation. All hydrogen cultures were grown on a wheel in the incubator. Additionally, all cultures were transferred for supplementary growth into hydrogen tubes to ensure the removal of all magnetosomes. Varying volumes (1mL, 0.5 mL, 0.2 mL, and 0.1 mL) of hydrogen grown cultures were transferred into nitrogen-infused medium, aiming to capture all stages of biomineralization more effectively. Optical density and magnetic response via $C_{mag}$ was monitored throughout growth as previously described [12] and at different stages of biomineralization samples were saved for TEM imaging. The progression of biomineralization stages was tracked using $C_{mag}$, with values ranging from 1.05 to 1.10 classified as early stages, 1.15 to 1.20 as middle stages, and 1.3 to 1.6 as late stages.

### Bacterial adenylate cyclase two-hybrid (BACTH) assays

The assay was performed as described in the Euromedex BACTH system kit manual. N- and C-terminal T18 and T25 fusions of Mad10, Mad20, Mad23, Mad25, Mad26, Mad28 and MamK proteins were constructed using plasmid pKT25, pKNT25, pUT18C, and pUT18 in *E. coli* K12 strain DH5-alpha. All plasmids were sequence-verified to show T18/T25 magnetosome protein fusions were correct. The fusions were then co-transformed into competent *E. coli* DHM1 cells (lacking endogenous adenylate cyclase activity) in all pairwise combinations, plated on LB agar plates containing 100 µg/mL carbenicillin and 50 µg/mL kanamycin, and incubated at 30 °C overnight. Several colonies of T18/T25 co-transformants were isolated and grown in LB liquid medium with 100 µg/mL carbenicillin and 50 µg/mL kanamycin overnight at 30 °C with 220 rpm shaking. Overnight cultures were spotted on indicator plates containing minimal M63/maltose medium with agar supplemented with 40 µg/mL X-gal, 50 µg/ml carbenicillin; and

25 µg/ml kanamycin. Plates were incubated 4 to 8 days at 30 °C before imaging. Bacteria expressing interacting hybrid proteins will show blue, while bacteria expressing non-interacting proteins will remain white. Different concentrations of IPTG (0, 0.1 mM and 0.5 mM) were tested in the overnight culture as well as on the indicator plates with little to no difference. Therefore, IPTG was not included in the final cultures and plates of this experiment.

## Electron microscopy

Whole-cell TEM imaging was performed as described previously [15]. All TEM was done using the Tecnai 12 at the EM-Lab at the University of California, Berkeley (https://em-lab.berkeley.edu/EML/index.php). Magnetosomes were measured manually using ImageJ. Cells were also counted manually.

## Acknowledgement

A.K. and V.V.R. are supported through the National Institute of General Medical Sciences (R35GM127114). The QB3/Chemistry Mass Spectrometry Facility at the University of California, Berkeley received support from the National Institutes of Health (grant 1S10OD020062-01). Additionally, V.V.R. was supported through the Genetics Training Grant, which receives funds from the National Institutes of Health (Grant #: 1T32GM132022). Thank you to the staff at the University of California Berkeley Electron Microscope Laboratory for advice and assistance in electron microscopy.

## Figures:

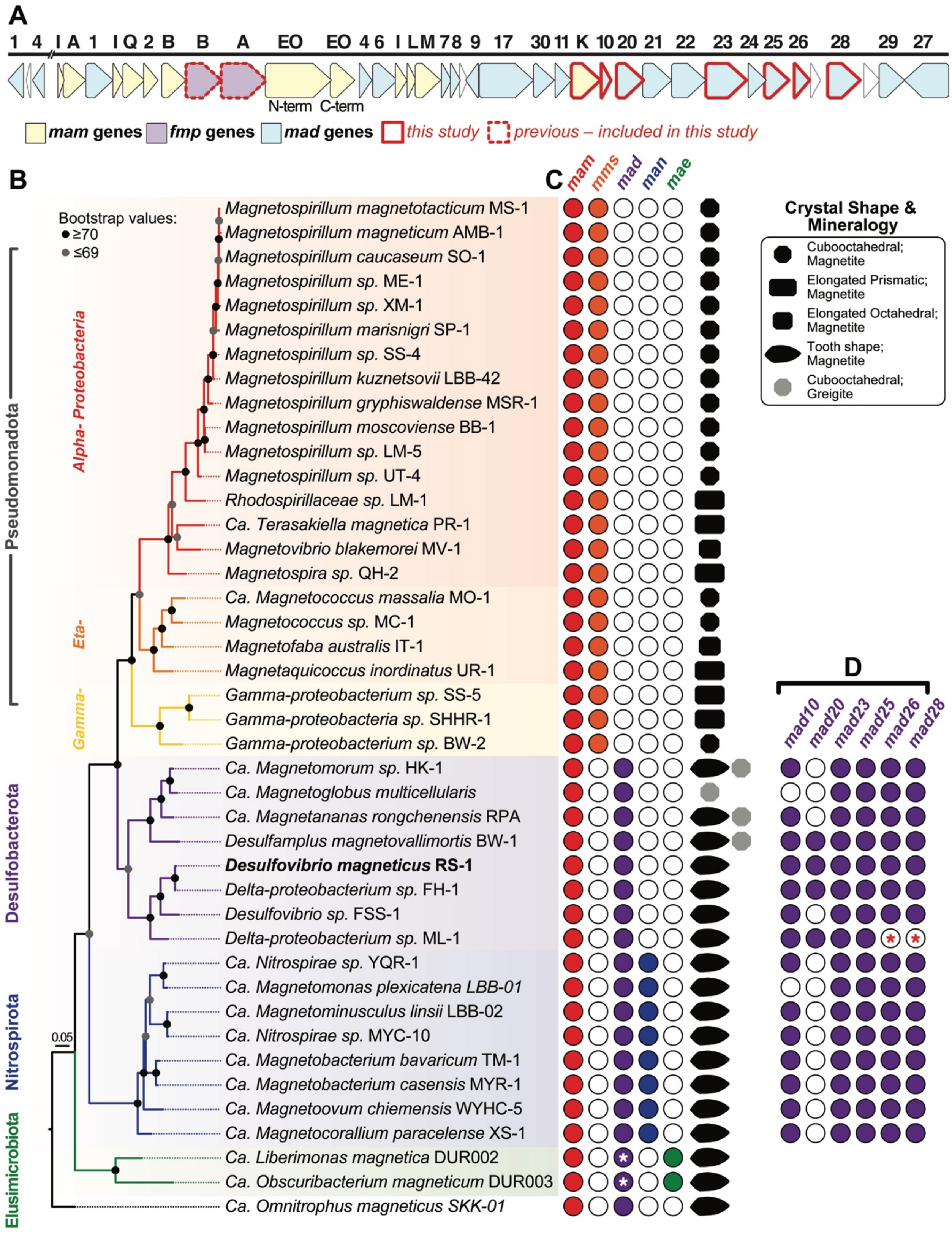
A
1 4 I A 1 I Q 2 B B A EO EO 4 6 I L M 7 8 9 17 30 11 K 10 20 21 22 23 24 25 26 28 29 27
N-term C-term
mam genes
fmp genes
mad genes
this study
previous – included in this study
B
C
mam
mms
mad
man
mae
Bootstrap values:
≥70
≤69
Pseudomonadota
Alpha- Proteobacteria
Eta-
Gamma-
Desulfobacterota
Nitrospirota
Elusimicrobiota
0.05
Magnetospirillum magnetotacticum MS-1
Magnetospirillum magneticum AMB-1
Magnetospirillum caucaseum SO-1
Magnetospirillum sp. ME-1
Magnetospirillum sp. XM-1
Magnetospirillum marisnigri SP-1
Magnetospirillum sp. SS-4
Magnetospirillum kuznetsovii LBB-42
Magnetospirillum gryphiswaldense MSR-1
Magnetospirillum moscoviense BB-1
Magnetospirillum sp. LM-5
Magnetospirillum sp. UT-4
Rhodospirillaceae sp. LM-1
Ca. Terasakiella magnetica PR-1
Magnetovibrio blakemorei MV-1
Magnetospira sp. QH-2
Ca. Magnetococcus massalia MO-1
Magnetococcus sp. MC-1
Magnetofaba australis IT-1
Magnetaquicoccus inordinatus UR-1
Gamma-proteobacterium sp. SS-5
Gamma-proteobacteria sp. SHHR-1
Gamma-proteobacterium sp. BW-2
Ca. Magnetomorum sp. HK-1
Ca. Magnetoglobus multicellularis
Ca. Magnetananas rongchenensis RPA
Desulfamplus magnetovallimortis BW-1
Desulfovibrio magneticus RS-1
Delta-proteobacterium sp. FH-1
Desulfovibrio sp. FSS-1
Delta-proteobacterium sp. ML-1
Ca. Nitrospirae sp. YQR-1
Ca. Magnetomonas plexicatena LBB-01
Ca. Magnetominusculus linsii LBB-02
Ca. Nitrospirae sp. MYC-10
Ca. Magnetobacterium bavaricum TM-1
Ca. Magnetobacterium casensis MYR-1
Ca. Magnetoovum chiemensis WYHC-5
Ca. Magnetocorallium paracelense XS-1
Ca. Liberimonas magnetica DUR002
Ca. Obscuribacterium magneticum DUR003
Ca. Omnitrophus magneticus SKK-01
Crystal Shape & Mineralogy
Cubooctahedral; Magnetite
Elongated Prismatic; Magnetite
Elongated Octahedral; Magnetite
Tooth shape; Magnetite
Cubooctahedral; Greigite
D
mad10
mad20
mad23
mad25
mad26
mad28

**Figure 1.** *Phylogenetic tree of MTB with their magnetosome gene composition and magnetosome crystal shape*

(A) Magnetosome gene cluster in RS-1. All *mam* genes are in yellow, all *mad* genes are in blue and *fmp* genes are in purple. Genes outlined in red (*mamK*, *mad10*, *mad20*, *mad23*, *mad25*, *mad26* and *mad28*) were the focus of this study. Outlined in dotted red (*fmpA* and *fmpB*) are genes mutated in a previous study[12], but examined further in this study. (B) 16S maximum likelihood tree. MAFFT was used for alignment of 16S genes. Maximum likelihood tree was built using PhyML Tree[39] with GTR substitution model and 1000 bootstraps. (C) For each MTB species the classification of the type of magnetosome genes (*mam*, *mms*, *mad*, *man* or *mae*) are provided as well as the magnetosome mineral composition and shape. White asterisks indicate the potential presence of *mad* genes, which were previously reported as missing[8] (*see Supplemental Figure S3-B*). (D) Deep-branching MTB species that contain the *mad* genes studied here. Red asterisks represent uncertainty due to a lack of a completed genome on NCBI. *Supplemental table 1* contains all the data (NCBI genome IDs, 16S gene ID and references) used to generate the phylogenetic tree (B), magnetosome gene information (A, C & D), and literature with crystal TEM images and chemical composition (C).

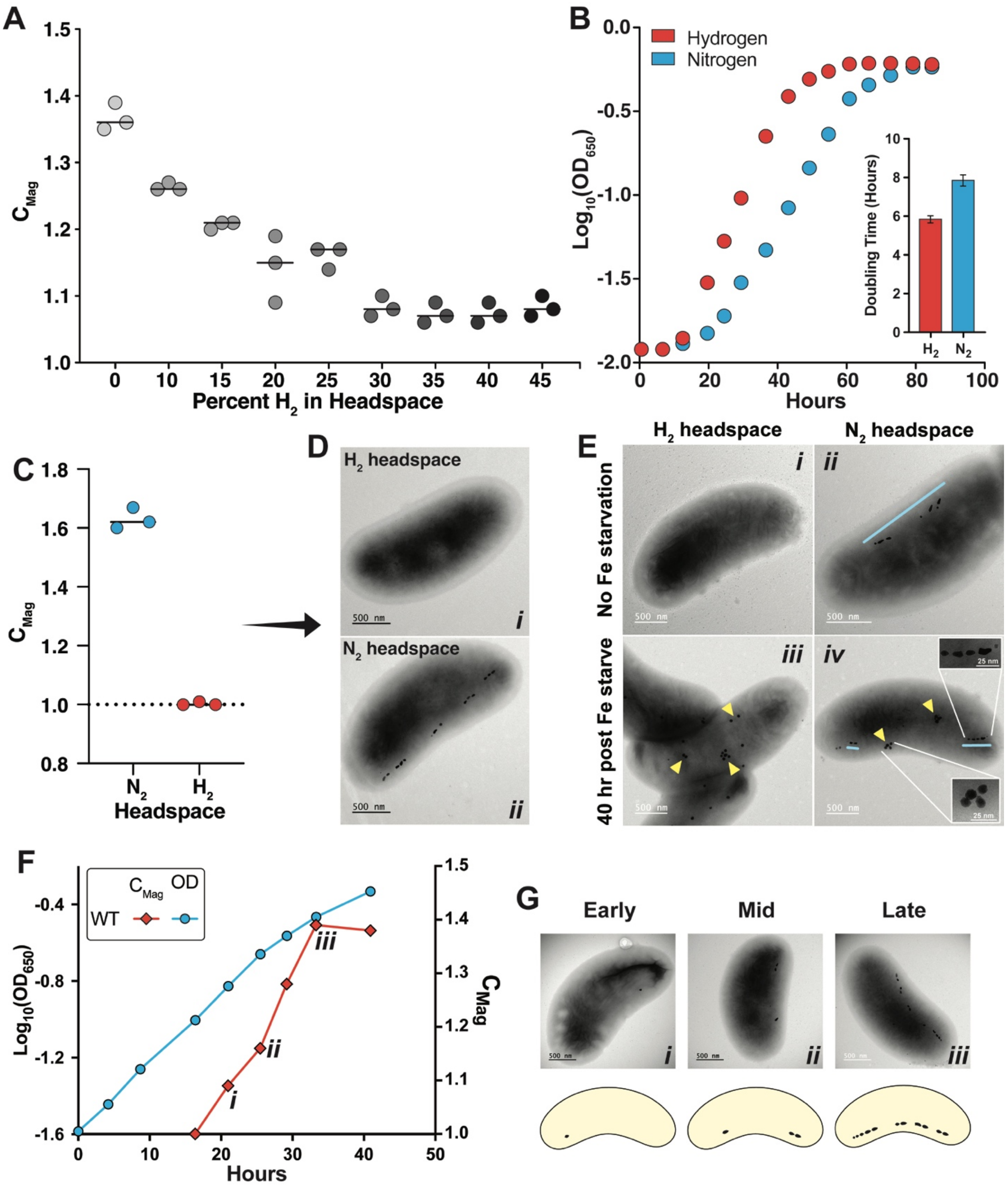

**Figure 2.** *Hydrogen inhibits magnetosome synthesis but not ferrosome production*

(A) Different concentration of hydrogen gas was added to the headspace and the magnetic response, $C_{mag}$ was measured over growth. (B) Growth curve of WT RS-1 grown with nitrogen (blue) or hydrogen (orange) in the headspace. Inlet graph shows the doubling time for both conditions. (C) RS-1 grown spinning on a wheel with either nitrogen (blue) or hydrogen (orange). $C_{mag}$ values indicate no magnetic response for cultures grown with hydrogen in the headspace. (D) TEM images of cultures from (C). (E) Initial cultures were either grown with or without iron to simulate iron starvation. Pre-cultures were transferred into either hydrogen or nitrogen conditions. (E*i*) TEM image of a cell grown in hydrogen with no iron starvation, (E *ii*) TEM image of a cell grown in nitrogen with no iron starvation, and (E *iii* and *iv*) are TEM images after iron starvation for cells grown in hydrogen (*iii*) or nitrogen (*iv*). Blue lines indicate magnetosomes and yellow triangles point to ferrosomes. (F) Growth curve (blue line) of a culture transitioning from hydrogen to nitrogen conditions to initiate biomineralization. The $C_{Mag}$ curve (orange line) of the same culture demonstrates biomineralization initiation and progression during growth. (F *i-iii*) indicate time points at which samples were collected for TEM imaging in (G *i-iii*).

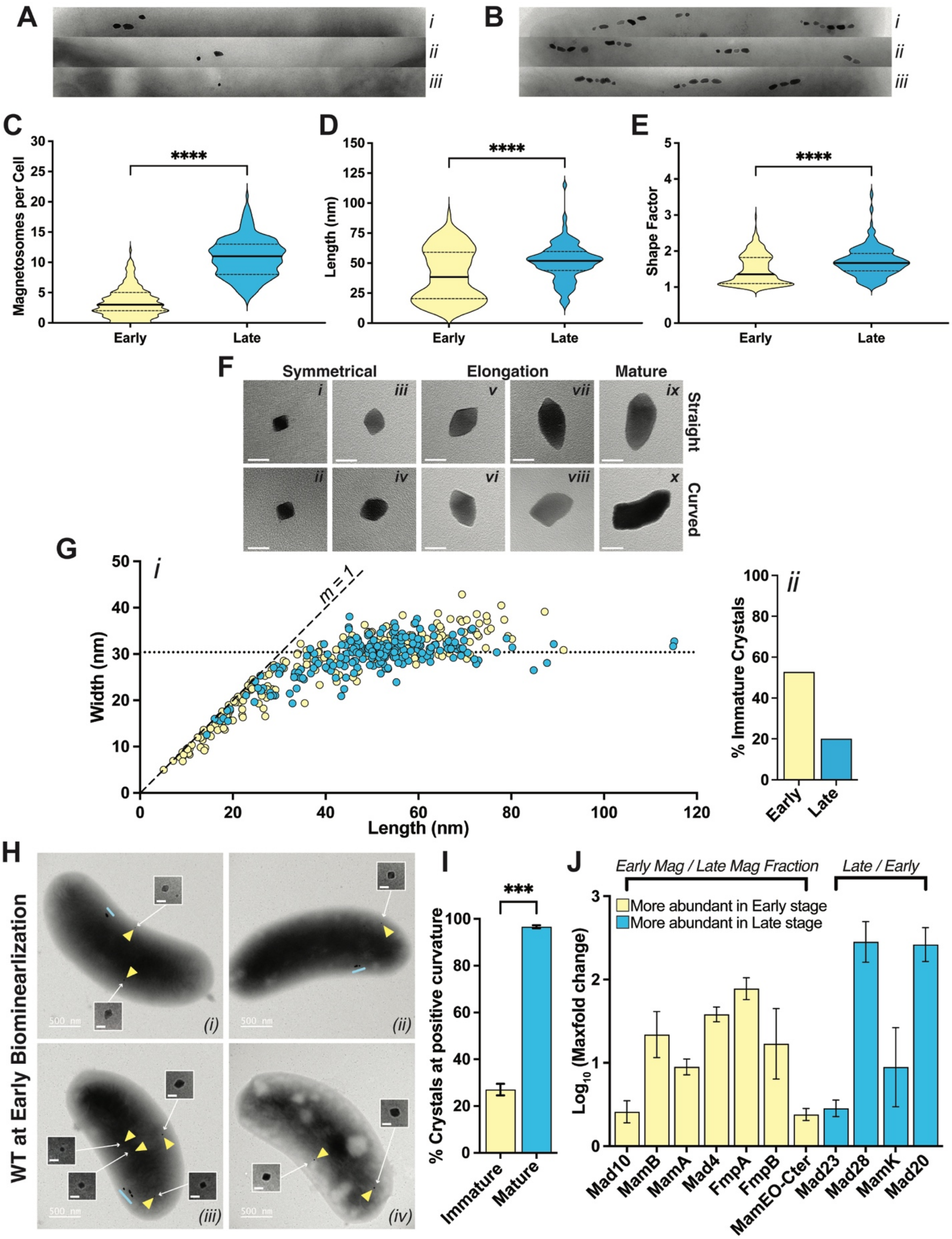

536

537 **Figure 3.** *Proteomic analysis of magnetosome proteins at different stages of biomineralization*

(A-B) TEM images of chains representing early and late stages of biomineralization. (C) Violin plots depicting the number of magnetosomes per cell for cells in early and late stages of biomineralization. (D) Violin plots illustrating measurements of magnetosome length and (E) shape factor (length/width) for crystals found in early and late stages of biomineralization, n=212 for early stages and n=214 for late stages. (F) TEM images of RS-1 magnetosomes at different stages of growth. All scale bars are 25 nm. (G) Each point is the measurement of the length and width of one crystal from WT (AK80). Yellow dots represent crystals from cells at early stages of biomineralization. Blue dots represent crystals from cells at late stages of biomineralization. The dotted line represents the median width of crystals from late stages of biomineralization. Dashed line shows a slope (*m*) of 1. (H) TEM images of early stage biomineralization of WT cells. Yellow triangles point to immature crystals that are included as zoomed-in images in the inset. Blue line indicates mature magnetosomes. The white scale bars for the zoomed-in crystals are all 25 nm. (I) The proportion of magnetosomes positioned at the positive curvature of the cell for both immature (yellow bar) and mature (blue bar) crystals during this stage, 140 cells counted; n=254 immature crystals, and n=394 mature crystals. (J) The $\log_{10}$ maximum fold change of magnetosome protein abundance detected in the crystal fraction at different stages of biomineralization. Yellow bars represent proteins more abundant at the early stage and blue bars represent proteins more abundant at the late stage of biomineralization.

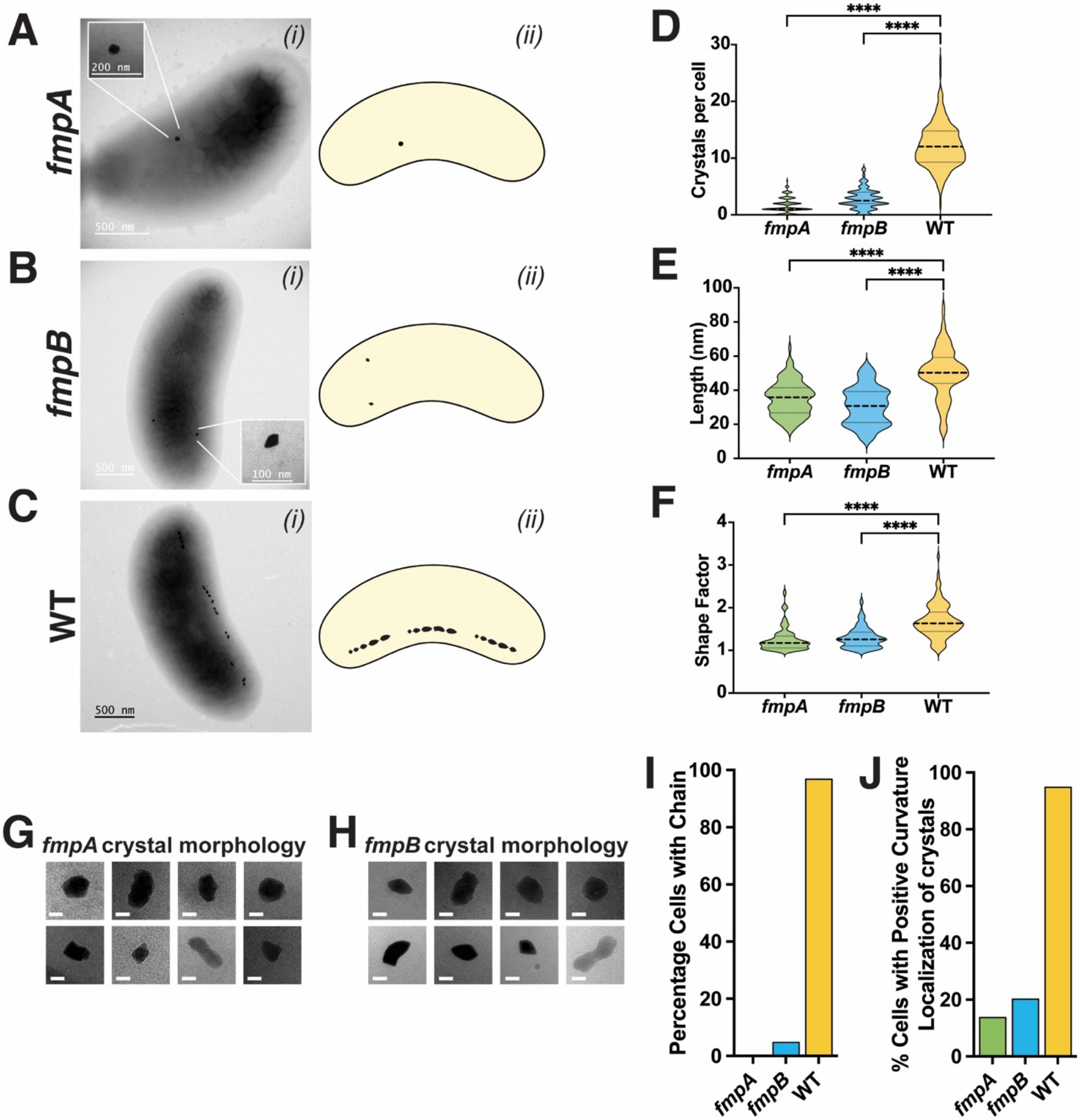

**Figure 4.** *Characterization of fmpA and fmpB mutants*

A-C) (*i*) TEM images of *fmpA* and *fmpB* mutant strains (scale bars 500 nm for main image and 100 nm for inset). (*ii*) Cartoon diagram of each strain. (D) Violin plots depicting the number of crystals per cell for each strain. (E) Violin plots illustrating measurements of magnetosome length, and (F) shape factor (length/width) for crystals in each strain. Data for (D), (E), and (F) are based on n=200 per strain. (G-H) Crystal morphology for each mutant, scale bars are 25 nm. (I) Percentage of cells exhibiting a chain phenotype, defined as having more than one crystal aligned in a row, for each strain. (J) Percent of cells with crystals located at the positive curvature in the cell. (I-J) Over 200 cells were counted.

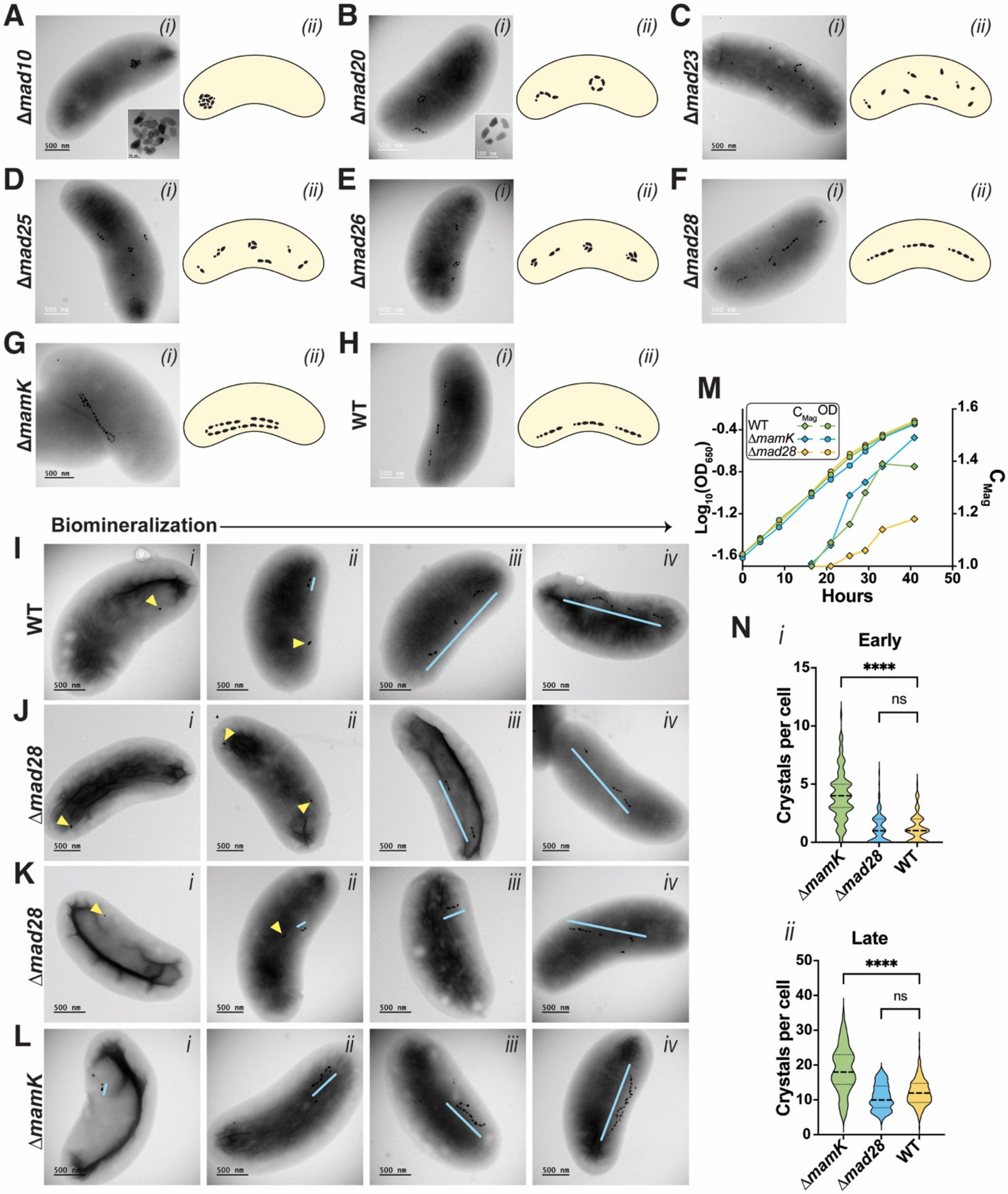

**Figure 5.** *Deletions of* mad *genes and mamK result in a variety of chain formation and localization defects*

(A-H) Phenotypes of different magnetosome gene deletion mutants and WT RS-1 with scale bars representing 500 nm. (*i*) is a TEM image ofor each strain and (*ii*) shows a cartoon diagram of representative magnetosome chain morphology. (I-L) TEM images of biomineralization time course of Δ*mad28*, Δ*mamK* and WT with scale bars representing 500 nm. Yellow triangles point at individual magnetosomes, whereas blue lines indicate chains or subchains of crystals. (I) Biomineralization time course of wildtype. (J) shows the phenotype for Δ*mad28* where the chain localizes to the mid-cell, whereas (K) shows the phenotype for Δ*mad28* where the chain localizes diagonally or transversally. (L) Biomineralization time course for Δ*mamK*, shows no subchains forming. (M) Growth curve and $C_{mag}$ curve for WT, Δ*mad28* and Δ*mamK*. (N *i*) Violin plots depicting the number of magnetosomes per cell for WT, Δ*mad28* and Δ*mamK* at early stages of biomineralization, over 100 cells counted for each strain. (N *ii*) Violin plots illustrating the number of magnetosomes per cell for WT, Δ*mad28* and Δ*mamK* at late stages of biomineralization, over 100 cells counted for each strain.

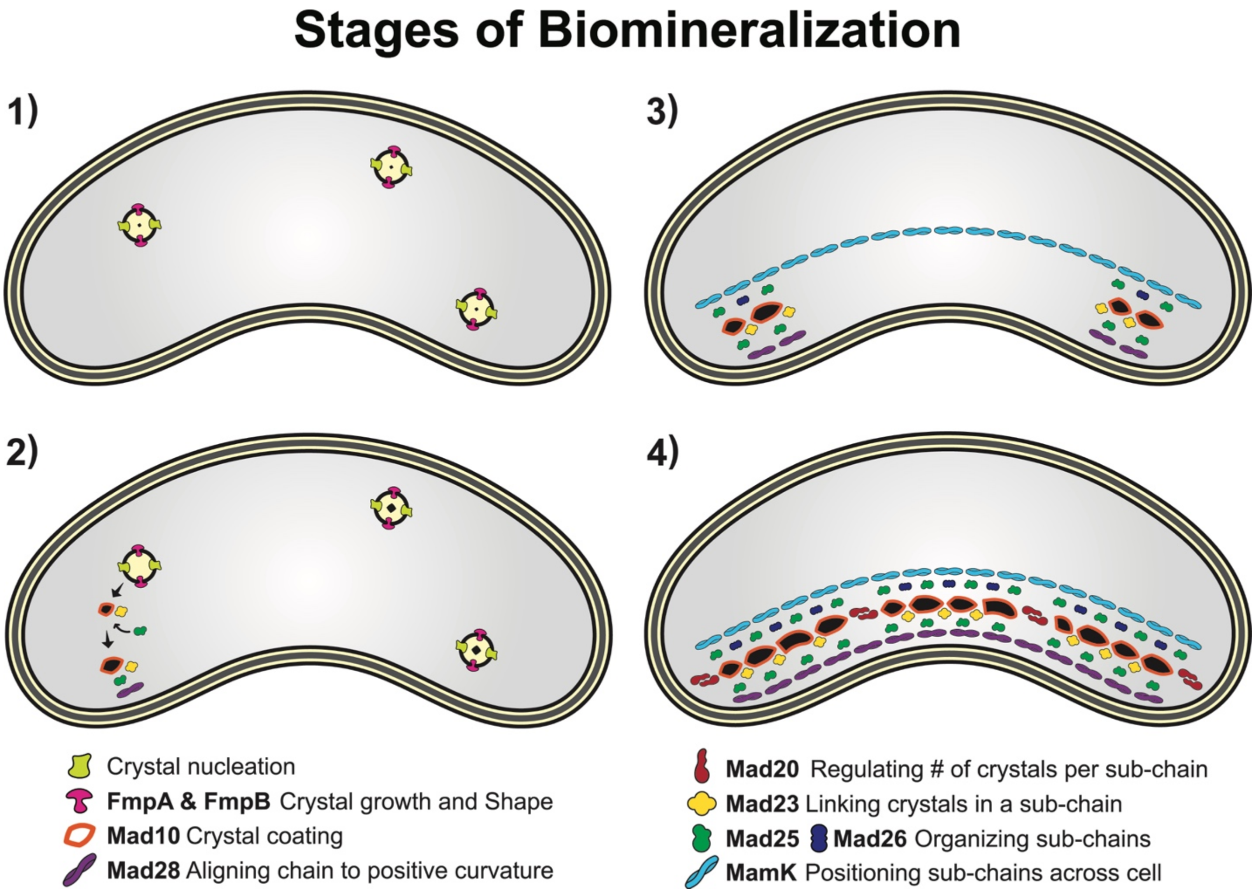

**Figure 6.** *Model of Magnetosome synthesis and chain organization in RS-1*

Model of the different stages of biomineralization in *Desulfovibrio magneticus* RS-1. ***Step 1:*** *Nucleation and Growth.* Biomineralization begins at nucleation sites randomly distributed within the cell. ***Step 2:*** *Crystal Maturation and Localization.* Maturing crystals are transported to the cell's positive curvature by a cohort of Mad proteins. ***Step 3:*** *Subchain Assembly.* As crystals reach the positive curvature, the process shifts to organizing them into subchains. ***Step 4:*** *Chain Elongation and Centering.* Subchains are extended and aligned along the cell length by MamK, while Mad28 ensures the chain remains localized at the positive curvature.

## References:

1. Amor, M., Mathon, F. P., Monteil, C. L., Busigny, V. & Lefevre, C. T. Iron-biomineralizing organelle in magnetotactic bacteria: function, synthesis and preservation in ancient rock samples. *Environmental Microbiology* **22**, 3611–3632 (2020).
2. Wan, J. *et al.* Biomineralization in magnetotactic bacteria: From diversity to molecular discovery-based applications. *Cell Reports* **43**, 114995 (2024).
3. Lefevre, C. T. & Bazylinski, D. A. Ecology, Diversity, and Evolution of Magnetotactic Bacteria. *Microbiology and Molecular Biology Reviews* **77**, 497–526 (2013).
4. Amor, M. *et al.* Magnetotactic Bacteria Accumulate a Large Pool of Iron Distinct from Their Magnetite Crystals. *Appl Environ Microbiol* **86**, e01278-20 (2020).
5. Vargas, G. *et al.* Applications of Magnetotactic Bacteria, Magnetosomes and Magnetosome Crystals in Biotechnology and Nanotechnology: Mini-Review. *Molecules* **23**, 2438 (2018).
6. Lin, W. *et al.* Genomic expansion of magnetotactic bacteria reveals an early common origin of magnetotaxis with lineage-specific evolution. *ISME Journal* **12**, 1508–1519 (2018).
7. Kolinko, I. *et al.* Biosynthesis of magnetic nanostructures in a foreign organism by transfer of bacterial magnetosome gene clusters. *Nature Nanotech* **9**, 193–197 (2014).
8. Uzun, M. *et al.* Recovery and genome reconstruction of novel magnetotactic Elusimicrobiota from bog soil. *The ISME Journal* **17**, 204–214 (2023).
9. Liu, P. *et al.* Key gene networks that control magnetosome biomineralization in magnetotactic bacteria. *National Science Review* **10**, nwac238 (2023).
10. Sakaguchi, T., Burgess, J. G. & Matsunaga, T. Magnetite formation by a sulphate-reducing bacterium. *Nature* **365**, 47–49 (1993).
11. Sakaguchi, T., Arakaki, A. & Matsunaga, T. Desulfovibrio magneticus sp. nov., a novel sulfate-reducing bacterium that produces intracellular single-domain-sized magnetite particles. *International Journal of Systematic and Evolutionary Microbiology* **52**, 215–221 (2002).
12. Rahn-Lee, L. *et al.* A Genetic Strategy for Probing the Functional Diversity of Magnetosome Formation. *PLoS Genet* **11**, e1004811 (2015).
13. Grant, C. R., Rahn-lee, L. & Legault, K. N. Genome Editing Method for the Anaerobic Magnetotactic. *Applied and Environmental Microbiology* **84**, 1–12 (2018).
14. Nakazawa, H. *et al.* Whole genome sequence of *Desulfovibrio magneticus* strain RS-1 revealed common gene clusters in magnetotactic bacteria. *Genome Res.* **19**, 1801–1808 (2009).

15. Byrne, M. E. *et al. Desulfovibrio magneticus* RS-1 contains an iron- and phosphorus-rich organelle distinct from its bullet-shaped magnetosomes. *Proc. Natl. Acad. Sci. U.S.A.* **107**, 12263–12268 (2010).
16. Komeili, A., Vali, H., Beveridge, T. J. & Newman, D. K. Magnetosome vesicles are present before magnetite formation, and MamA is required for their activation. *Proc. Natl. Acad. Sci. U.S.A.* **101**, 3839–3844 (2004).
17. Grant, C. R. *et al.* Distinct gene clusters drive formation of ferrosome organelles in bacteria. *Nature* **606**, 160–164 (2022).
18. Pi, H. *et al.* Clostridioides difficile ferrosome organelles combat nutritional immunity. *Nature* **623**, 1009–1016 (2023).
19. Schüler, D., Uhl, R. & Bäuerlein, E. A simple light scattering method to assay magnetism in *Magnetospirillum gryphiswaldense*. *FEMS Microbiology Letters* **132**, 139–145 (1995).
20. Li, J. *et al.* Crystal growth of bullet-shaped magnetite in magnetotactic bacteria of the *Nitrospirae* phylum. *J. R. Soc. Interface.* **12**, 20141288 (2015).
21. Komeili, A., Li, Z., Newman, D. K. & Jensen, G. J. Magnetosomes Are Cell Membrane Invaginations Organized by the Actin-Like Protein MamK. *Science* **311**, 242–245 (2006).
22. Pohl, A. *et al.* Decoding Biomineralization: Interaction of a Mad10-Derived Peptide with Magnetite Thin Films. *Nano Lett.* **19**, 8207–8215 (2019).
23. Pohl, A. *et al.* Magnetite-binding proteins from the magnetotactic bacterium *Desulfamplus magnetovallimortis* BW-1. *Nanoscale* **13**, 20396–20400 (2021).
24. Wan, J. *et al.* McaA and McaB control the dynamic positioning of a bacterial magnetic organelle. *Nat Commun* **13**, 5652 (2022).
25. Abreu, N. *et al.* Interplay between Two Bacterial Actin Homologs, MamK and MamK-Like, Is Required for the Alignment of Magnetosome Organelles in Magnetospirillum magneticum AMB-1. *J Bacteriol* **196**, 3111–3121 (2014).
26. Toro-Nahuelpan, M. *et al.* Segregation of prokaryotic magnetosomes organelles is driven by treadmilling of a dynamic actin-like MamK filament. *BMC Biol* **14**, 88 (2016).
27. Taoka, A. *et al.* Tethered Magnets Are the Key to Magnetotaxis: Direct Observations of *Magnetospirillum magneticum* AMB-1 Show that MamK Distributes Magnetosome Organelles Equally to Daughter Cells. *mBio* **8**, e00679-17 (2017).
28. Katzmann, E., Scheffel, A., Gruska, M., Plitzko, J. M. & Schüler, D. Loss of the actin-like protein MamK has pleiotropic effects on magnetosome formation and chain assembly in *Magnetospirillum gryphiswaldense*. *Molecular Microbiology* **77**, 208–224 (2010).

29. Awal, R. P. *et al.* Experimental analysis of diverse actin-like proteins from various magnetotactic bacteria by functional expression in *Magnetospirillum gryphiswaldense*. *mBio* **14**, e01649-23 (2023).
30. Liu, Y., Van Den Ent, F. & Löwe, J. Filament structure and subcellular organization of the bacterial intermediate filament–like protein crescentin. *Proc. Natl. Acad. Sci. U.S.A.* **121**, e2309984121 (2024).
31. Fields, S. & Song, O. A novel genetic system to detect protein–protein interactions. *Nature* **340**, 245–246 (1989).
32. Müller, F. D., Schüler, D. & Pfeiffer, D. A Compass To Boost Navigation: Cell Biology of Bacterial Magnetotaxis. *J Bacteriol* **202**, (2020).
33. Bickley, C. D., Wan, J. & Komeili, A. Intrinsic and extrinsic determinants of conditional localization of Mms6 to magnetosome organelles in *Magnetospirillum magneticum* AMB-1. *J Bacteriol* **206**, e00008-24 (2024).
34. Arakaki, A. *et al.* Comparative Subcellular Localization Analysis of Magnetosome Proteins Reveals a Unique Localization Behavior of Mms6 Protein onto Magnetite Crystals. *J Bacteriol* **198**, 2794–2802 (2016).
35. Chariaou, M. *et al.* Anisotropy of Bullet-Shaped Magnetite Nanoparticles in the Magnetotactic Bacteria Desulfovibrio magneticus sp. Strain RS-1. *Biophysical Journal* **108**, 1268–1274 (2015).
36. Kovács, A. *et al.* Influence of crystal shape and orientation on the magnetic microstructure of bullet-shaped magnetosomes synthesized by magnetotactic bacteria. *Geo-bio interfaces* **1**, e1 (2024).
37. Chen, I.-M. A. *et al.* The IMG/M data management and analysis system v.7: content updates and new features. *Nucleic Acids Research* **51**, D723–D732 (2023).
38. Katoh, K. & Standley, D. M. MAFFT multiple sequence alignment software version 7: improvements in performance and usability. *Mol Biol Evol* **30**, 772–780 (2013).
39. Guindon, S. *et al.* New algorithms and methods to estimate maximum-likelihood phylogenies: assessing the performance of PhyML 3.0. *Syst Biol* **59**, 307–321 (2010).
40. Constant Systems | Multi Cycle Cell Disruptor. *Constant Systems* https://constantsystems.com/products/multi-cycle-cell-disruptor/.
41. Ehrlich, H., Bailey, E., Wysokowski, M. & Jesionowski, T. Forced Biomineralization: A Review. *Biomimetics* **6**, 46 (2021).

## Extended Results:

### Protein abundance during hydrogen-induced inhibition of magnetosome synthesis

We investigated whether hydrogen affects magnetosome protein expression by comparing proteomes of RS-1 cultures grown in hydrogen or nitrogen using liquid chromatography-mass spectrometry. Most magnetosome gene cluster (MGC) proteins showed similar levels, except Mad10, which was over 20 times more abundant in nitrogen (Supplemental Figure S8-B). However, Mad10 is not responsible for magnetosome inhibition under hydrogen conditions, as indicated by its magnetosome formation phenotype. In hydrogen-grown cells, hydrogenases, a response regulator, a signaling protein, and the ferric uptake regulator, Fur, were more abundant, while nitrogen-grown cells had higher levels of dehydrogenases and a carbon storage regulator (Supplemental Figure S8 C-F). These findings suggest potential molecular mechanisms for hydrogen's effect on magnetosome formation, warranting further investigation in the future.

### Architecture of Chain organization proteins in RS-1

For each chain organization gene deleted in RS-1, predicted protein structures were modeled to visualize their structural features. Mad20, Mad25, and Mad26 all exhibited similar protein structures, characterized by long coiled-coil filament-like regions (Supplemental Figure S5 C-E), resembling the coiled-coil protein, Crescentin, found in *Caulobacter crescentus*[1]. These coiled-coil domains are predicted to facilitate strong protein-protein interactions, which was supported by bacterial two-hybrid assays, where all three proteins interacted extensively with each other as well as with other chain organization proteins (Supplemental Figure S2). Mad10 and Mad23, in contrast, have much shorter coiled-coil regions (Supplemental Figure S3A), which is also reflected in their 3D structural models (Supplemental Figure S5 A-B). While Mad10 lacks additional predicted domains, previous studies suggest it contains a magnetite-binding region[2]. Mad23, however, possesses a distinctive HEAT repeat domain in addition to its small coiled-coil region (Supplemental Figure S5 B-ii). HEAT domains are typically associated with protein-protein interactions, a hypothesis further supported by bacterial two-hybrid assays, where Mad23 showed strong interactions with Mad10 and Mad25 (Supplemental Figure S2).

Both Mad28 and MamK are predicted to contain actin-like domains and share highly similar predicted protein structures (Supplemental Figure S5 F-G). To further investigate their relationship, we performed both 3D structural and protein sequence alignments. While the sequence alignment revealed low similarity, the 3D structural alignment showed strong alignment between the two proteins, suggesting that despite sequence divergence, their structural similarities may indicate conserved functions. However, our genetic studies and biomineralization time course analyses revealed distinct roles: MamK is essential for sub-chain formation, while Mad28 is required for proper chain localization along the positive curvature (Figure 5F-G). Additionally, the original *mad28* sequence from RS-1 in the NCBI database before 2019 lacked the first 114 nucleotides or 38 amino acids, shown in green in Supplemental Figure S5 H-J. However, this region is essential for restoring the wild-type phenotype in *mad28* complementation experiments. Notably, this sequence is unique to Mad28 and does not align with MamK in the 3D structural comparison (Supplemental Figure S5-H). This specific *mad28* region is also present in Mad28 homologs from other deep-branching MTB, further supporting its functional significance. Supplemental Figure S5-I highlights this region in green in MYR-1, a deep-branching MTB from the *Nitrospirota* phylum.

## Extended data Figures:

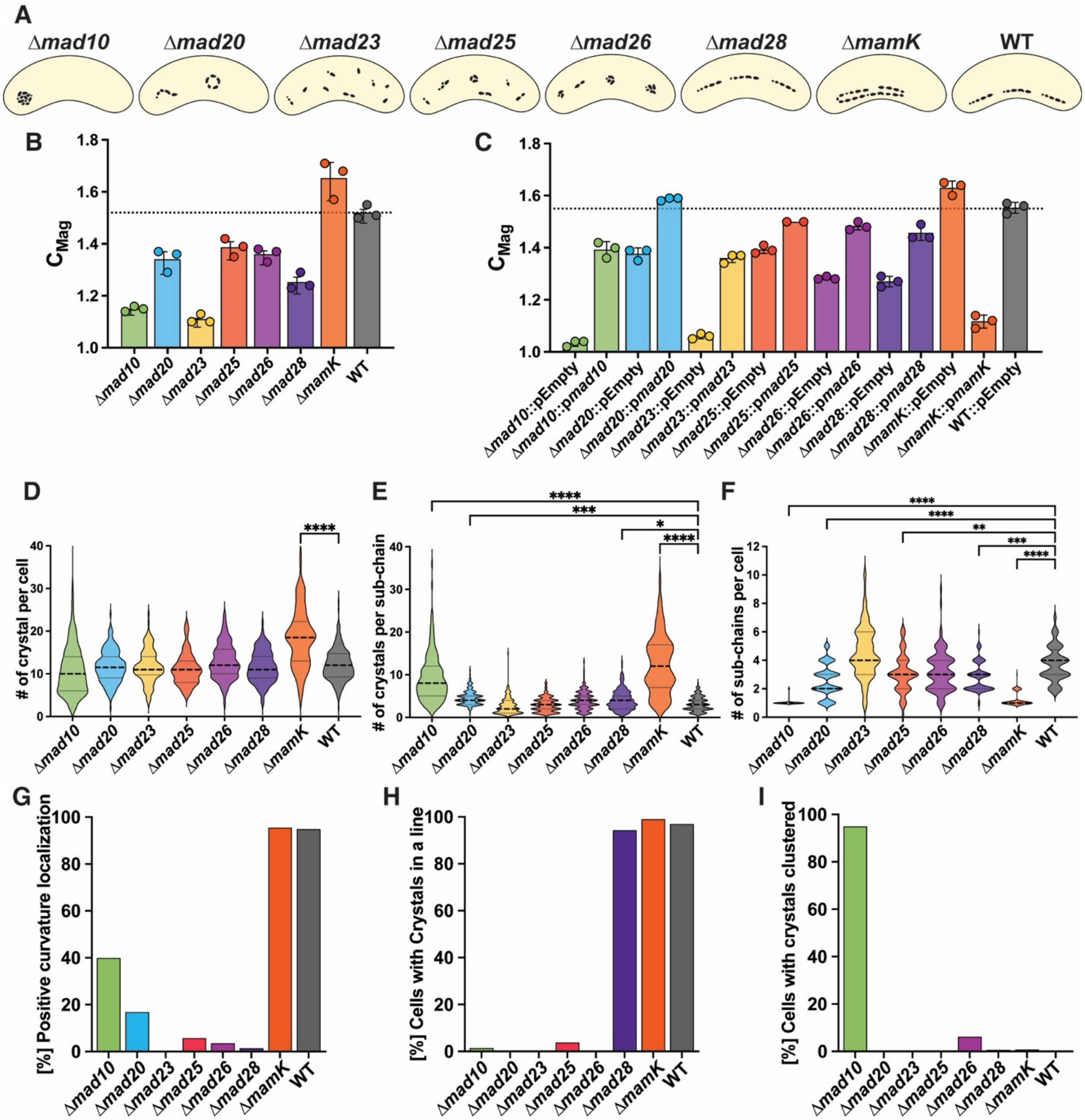

**Supplemental S1.** *Characterization of magnetosome gene deletions in RS-1*

(A) Cartoon diagram of representative phenotype of each strain. (B) $C_{Mag}$ values for each strain, with cultures grown in triplicate. No plasmids were present in the cells. Error bars indicate standard deviation. (C) $C_{Mag}$ values for each mutant with an empty plasmid and for each mutant with a plasmid constitutively expressing the deleted gene. The WT strain carries only an empty plasmid. The dotted line in (B) and (C) represents the average $C_{Mag}$ of WT. (D) Violin plots displaying the number of crystals per cell for each strain. (E) Violin plots illustrating the number of crystals per subchain for each strain. (F) Violin plots representing the number of subchains per cell for each strain. All statistical tests used on (D), (E), and (F) are stated in *Supplemental table 8*. (G-I) The percentage of cells exhibiting specific phenotypes, based on a count of 200 cells per strain. (G) The percentage of cells with crystals localized at the positive curvature of the cell, (H) shows the percentage of cells with magnetosomes displaying a chain phenotype, and (I) indicates the percentage of cells with all magnetosomes in the cell clustered together.

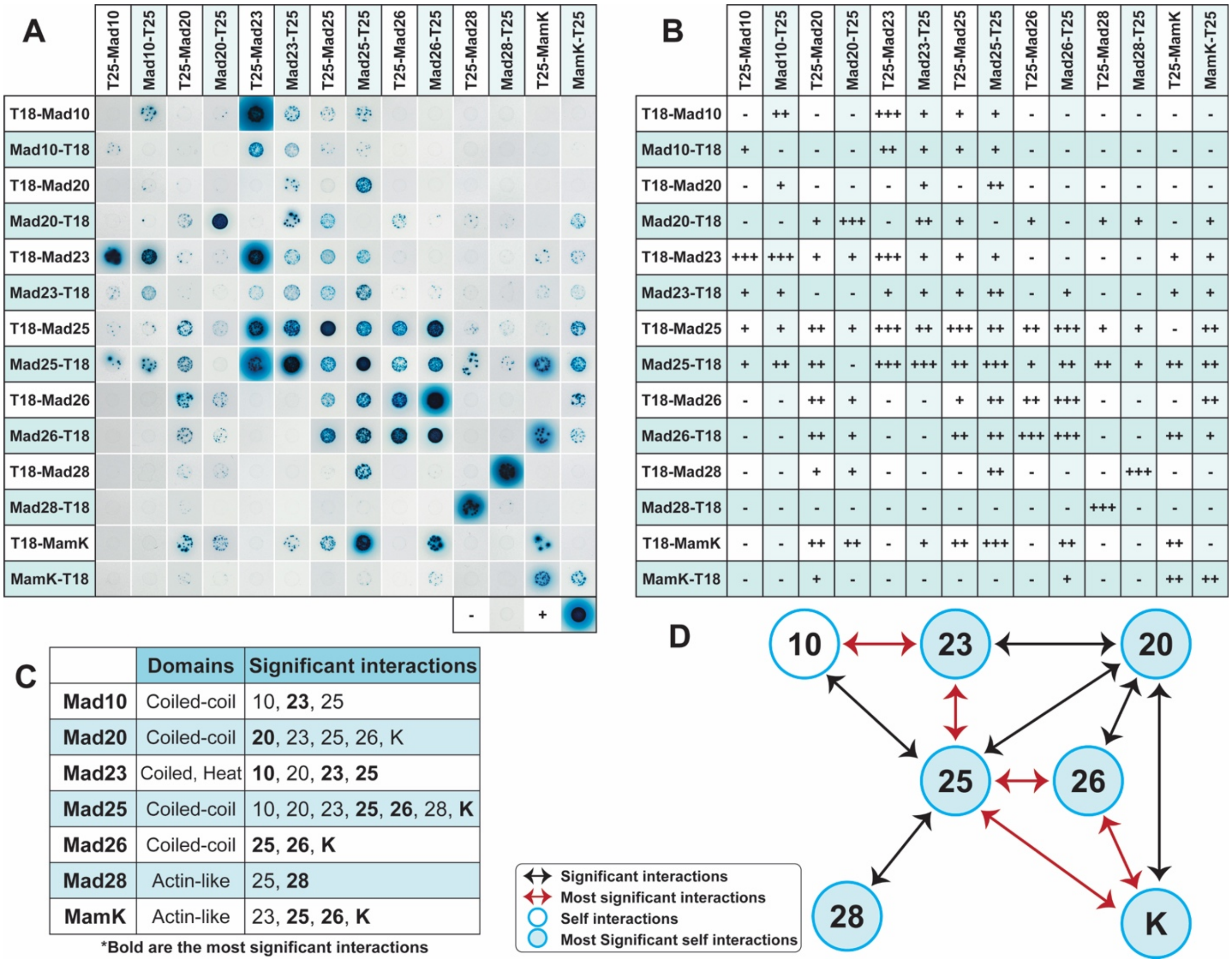

B

|  | T25-Mad10 | Mad10-T25 | T25-Mad20 | Mad20-T25 | T25-Mad23 | Mad23-T25 | T25-Mad25 | Mad25-T25 | T25-Mad26 | Mad26-T25 | T25-Mad28 | Mad28-T25 | T25-MamK | MamK-T25 |
|---|---|---|---|---|---|---|---|---|---|---|---|---|---|---|
| T18-Mad10 | - | ++ | - | - | +++ | + | + | + | - | - | - | - | - | - |
| Mad10-T18 | + | - | - | - | ++ | + | + | + | - | - | - | - | - | - |
| T18-Mad20 | - | + | - | - | - | + | - | ++ | - | - | - | - | - | - |
| Mad20-T18 | - | - | + | +++ | - | ++ | + | - | + | - | + | + | - | + |
| T18-Mad23 | +++ | +++ | + | + | +++ | + | + | + | - | - | - | - | + | + |
| Mad23-T18 | + | + | - | - | + | + | + | ++ | - | + | - | - | + | + |
| T18-Mad25 | + | + | ++ | + | +++ | ++ | +++ | ++ | ++ | +++ | + | + | - | ++ |
| Mad25-T18 | + | ++ | ++ | - | +++ | +++ | ++ | +++ | + | ++ | ++ | + | ++ | ++ |
| T18-Mad26 | - | - | ++ | + | - | - | + | ++ | ++ | +++ | - | - | - | ++ |
| Mad26-T18 | - | - | ++ | + | - | - | ++ | ++ | +++ | +++ | - | - | ++ | + |
| T18-Mad28 | - | - | + | + | - | - | - | ++ | - | - | - | +++ | - | - |
| Mad28-T18 | - | - | - | - | - | - | - | - | - | - | +++ | - | - | - |
| T18-MamK | - | - | ++ | ++ | - | + | ++ | +++ | - | ++ | - | - | ++ | - |
| MamK-T18 | - | - | + | - | - | - | - | - | - | + | - | - | ++ | ++ |

C

|  | Domains | Significant interactions |
|---|---|---|
| **Mad10** | Coiled-coil | 10, **23**, 25 |
| **Mad20** | Coiled-coil | **20**, 23, 25, 26, K |
| **Mad23** | Coiled, Heat | **10**, 20, **23**, **25** |
| **Mad25** | Coiled-coil | 10, 20, 23, **25**, **26**, 28, **K** |
| **Mad26** | Coiled-coil | **25**, **26**, **K** |
| **Mad28** | Actin-like | 25, **28** |
| **MamK** | Actin-like | 23, **25**, **26**, **K** |

*Bold are the most significant interactions

- ⟷ Significant interactions
- ⟷ Most significant interactions
- ○ Self interactions
- ● Most Significant self interactions

**Supplemental S2.** *Interactions of magnetosome chain organization proteins*

A Bacterial Adenylate Cyclase Two-Hybrid (BACTH) assay was conducted to assess interactions among magnetosome chain organization proteins—Mad10, Mad20, Mad23, Mad25, Mad26, Mad28, and MamK. Co-transformed E. coli DHM1 expressing T18- and T25-fusion proteins were spotted onto M63 maltose-mineral salts agar, where blue coloration indicates high β-galactosidase activity, signifying a positive interaction, while white indicates no interaction.

The positive control (leucine zipper) resulted in dark blue spots, while the negative controls (empty vector combinations) produced white spots, as expected. (A) Photographic images of spots for each interaction combination. (B) A table summarizing all interaction combinations, scored based on results from (A) and categorized by color intensity: dark blue spots indicate strong interaction (+++), medium blue spots represent moderate (++), light blue spots signify minor (+), and white denotes no interaction (-). (C) A table highlighting the most significant interactions. (D) A visual diagram illustrating these interactions: black arrows represent medium interactions, including bidirectional interactions (fusion with T25 and T18 interacting with their corresponding fusion partners), red arrows highlight strong bidirectional interactions, open blue circles indicate observed self-interactions, and filled blue circles denote strong self-interactions.

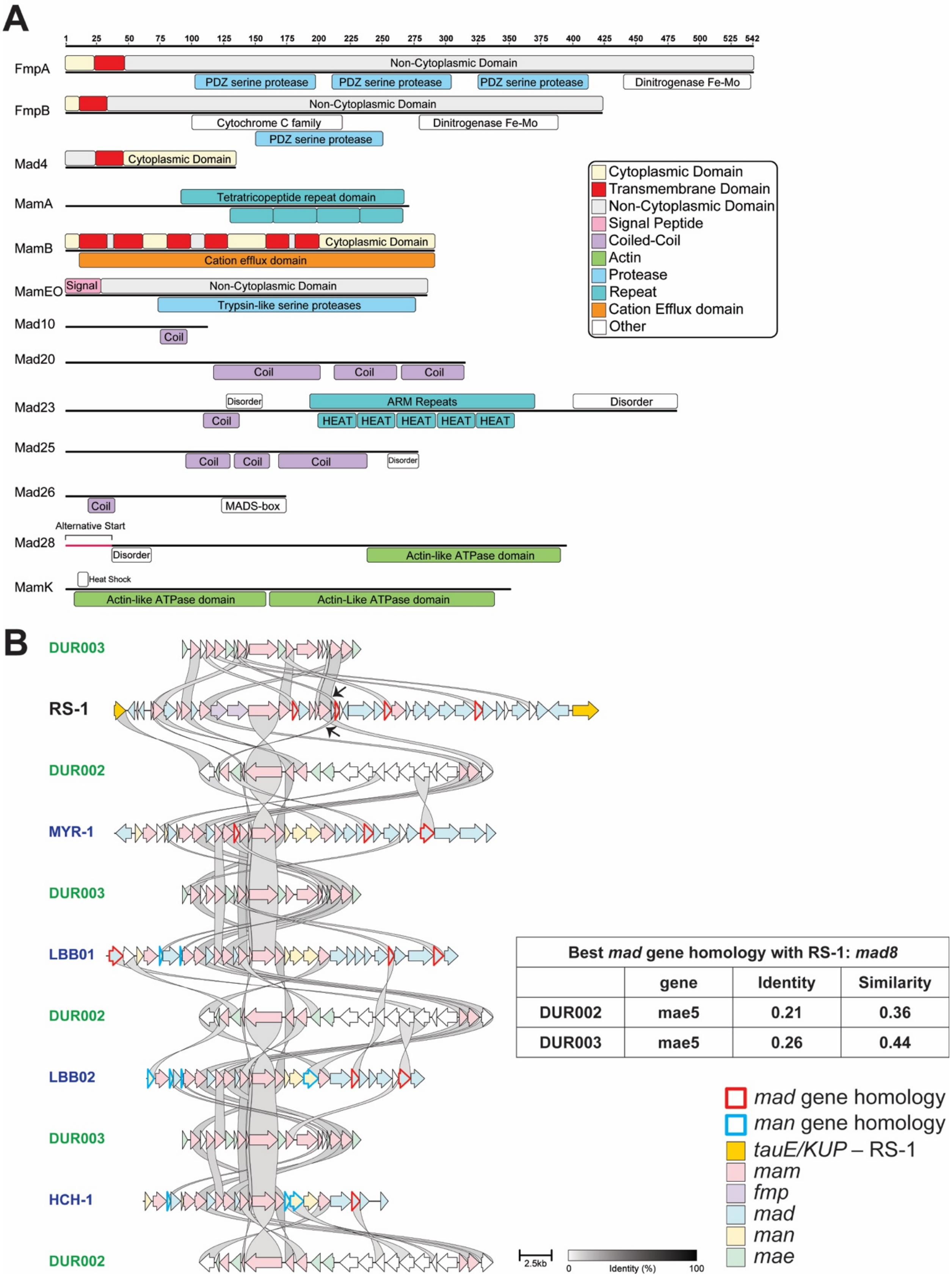

| Best *mad* gene homology with RS-1: *mad8* | | | |
|---|---|---|---|
| | gene | Identity | Similarity |
| DUR002 | mae5 | 0.21 | 0.36 |
| DUR003 | mae5 | 0.26 | 0.44 |

**Supplemental S3.** *Protein domains of magnetosome genes in this study and mad gene comparisons between deep branching MTB.*

(A) Domains of proteins studied here. Protein domains were identified using InterPro [3] and uploaded on to Geneious [4] to generate domain maps. Mad28 shows an alternative start site that was not included in the original NCBI annotation and ∆*mad28* could only be complemented when including the alternative start site. (B) Magnetosome gene cluster comparison between DUR002 and DUR003 *(Elusimicrobiota)* and RS-1 *(Desulfobacterota* representative*),* and between DUR002 and DUR003 and MYR-1, LBB01, LBB02, and HCH-1 *(Nitrospirota* representatives*)*. This analysis is to indicate, while DUR002 and DUR003 are stated to not contain any mad genes[5] they do have homologues to some *mad* genes. Magnetosome gene clusters were extracted from genomes available on NCBI manually and Clinker[6] was used to compare the MGCs. Genes outlined in red are *mad* genes that show some homology in either DUR002 or DUR003. Genes outlined in blue are *man* genes that show some homology in either DUR002 or DUR003. The table on the right shows the proportions of identity and similarity for homology of *mad8*, which was found to have homologs in both DUR002 and DUR003. The black arrows indicate the *mad8* homology on the comparison map. *mad4*, *mad11* and *mad24* from RS-1 also had homologs, but only in DUR003. In addition, *mad24* has a homolog to DUR003 in two *Nitrospirota* representatives, HCH-1 and LBB02.

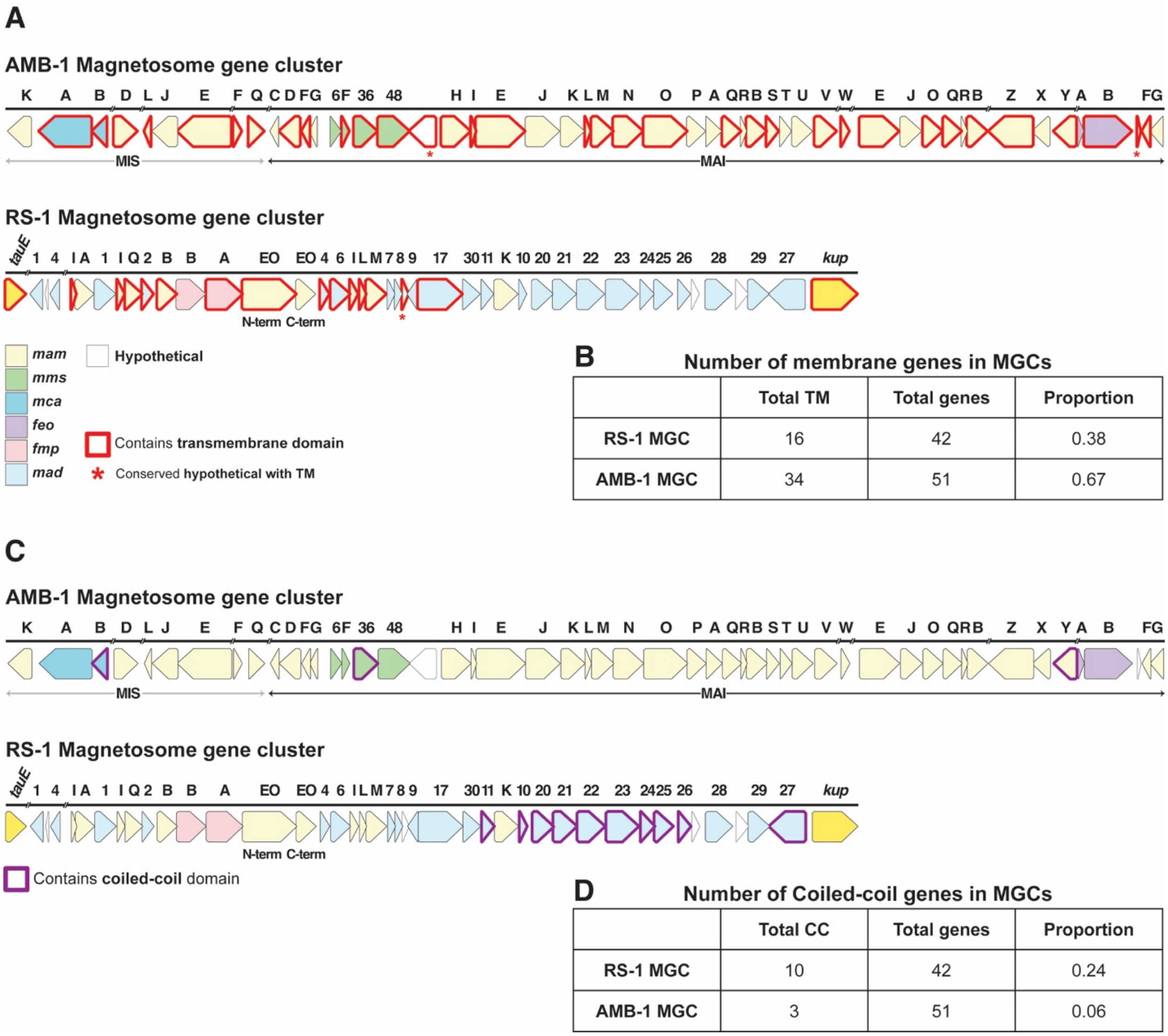

**B** Number of membrane genes in MGCs

| | Total TM | Total genes | Proportion |
|---|---|---|---|
| RS-1 MGC | 16 | 42 | 0.38 |
| AMB-1 MGC | 34 | 51 | 0.67 |

**D** Number of Coiled-coil genes in MGCs

| | Total CC | Total genes | Proportion |
|---|---|---|---|
| RS-1 MGC | 10 | 42 | 0.24 |
| AMB-1 MGC | 3 | 51 | 0.06 |

**Supplemental S4.** *Magnetosome gene cluster comparison between AMB-1 and RS-1.* (A) Magnetosome gene clusters in AMB-1 and RS-1. Genes highlighted in red encode for proteins with predicted transmembrane domains. (B) Table of the proportions of proteins with predicted transmembrane domains to all proteins encoded by the magnetosome gene clusters of AMB-1 and RS-1. TMHMM[7] was used to gather transmembrane domain predictions. (C) Magnetosome gene cluster of AMB-1 and RS-1 with genes encoding proteins with predicted coiled-coil domains highlighted in purple. (D) Table of the proportions of proteins with coiled-coil domains compared to all proteins in the MGC for AMB-1 and RS-1. DeepCoil[8] was used to obtain coiled-coil predictions.

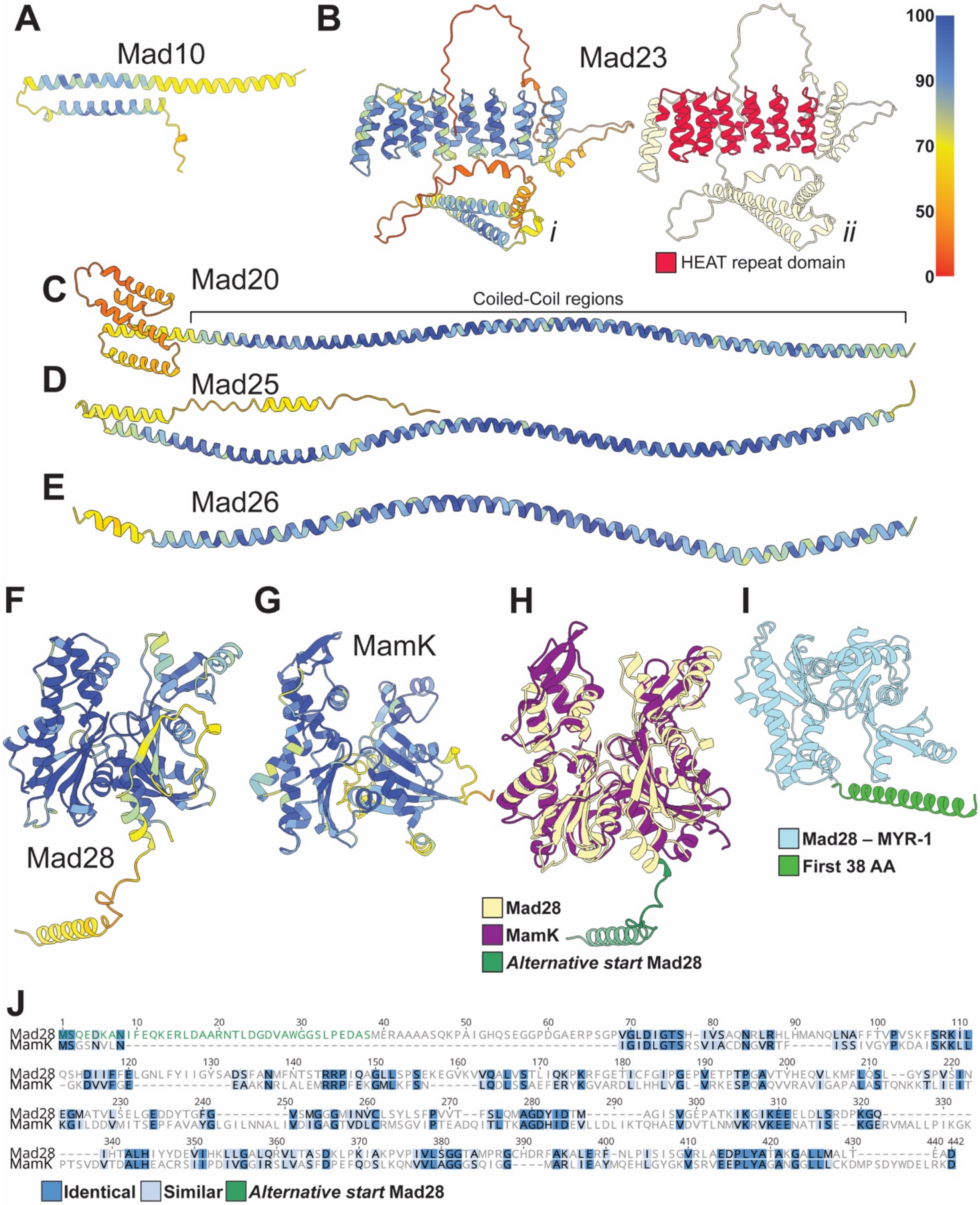

**Supplemental S5.** *Predicted 3D Structures of magnetosome proteins deleted in RS-1 and alignments of MamK and Mad28*

(A-I) Predicted protein structures of Mad proteins and MamK in this study were made with Alphafold3[9] and visualized with ChimeraX[10]. 3D structures are colored according to Alphafold confidence values, with blue at 100% confident and red 0% confidence. (B-*ii*) Indicates the location of the HEAT domain (colored in red) in Mad23. (H) 3D alignment of protein structures of Mad28 and MamK from RS-1. Protein structures were made with alphafold3 and then a 3D alignment was preformed using ChimeraX[10]. Purple is the 3D predicted structure for MamK, yellow is the predicted structure for Mad28 and green is the part of the structure that includes the alternative start site for Mad28. Δ*mad28* would only complement with this sequence included in the plasmid. (I) Predicted 3D structure of Mad28 from MYR-1, a deep-branching MTB in the *Nitrospirota* phylum. The first 38 amino acids are highlighted in green to indicate structural similarity to the corresponding region in RS-1's Mad28. (J) 2D protein sequence alignment of MamK and Mad28 using MAFFT v7.490 plug-in on Geneious[4]. Blue highlighted residues show similarities between sequences and dashes represent gaps. Green letters show the sequence for the alternative start in Mad28.

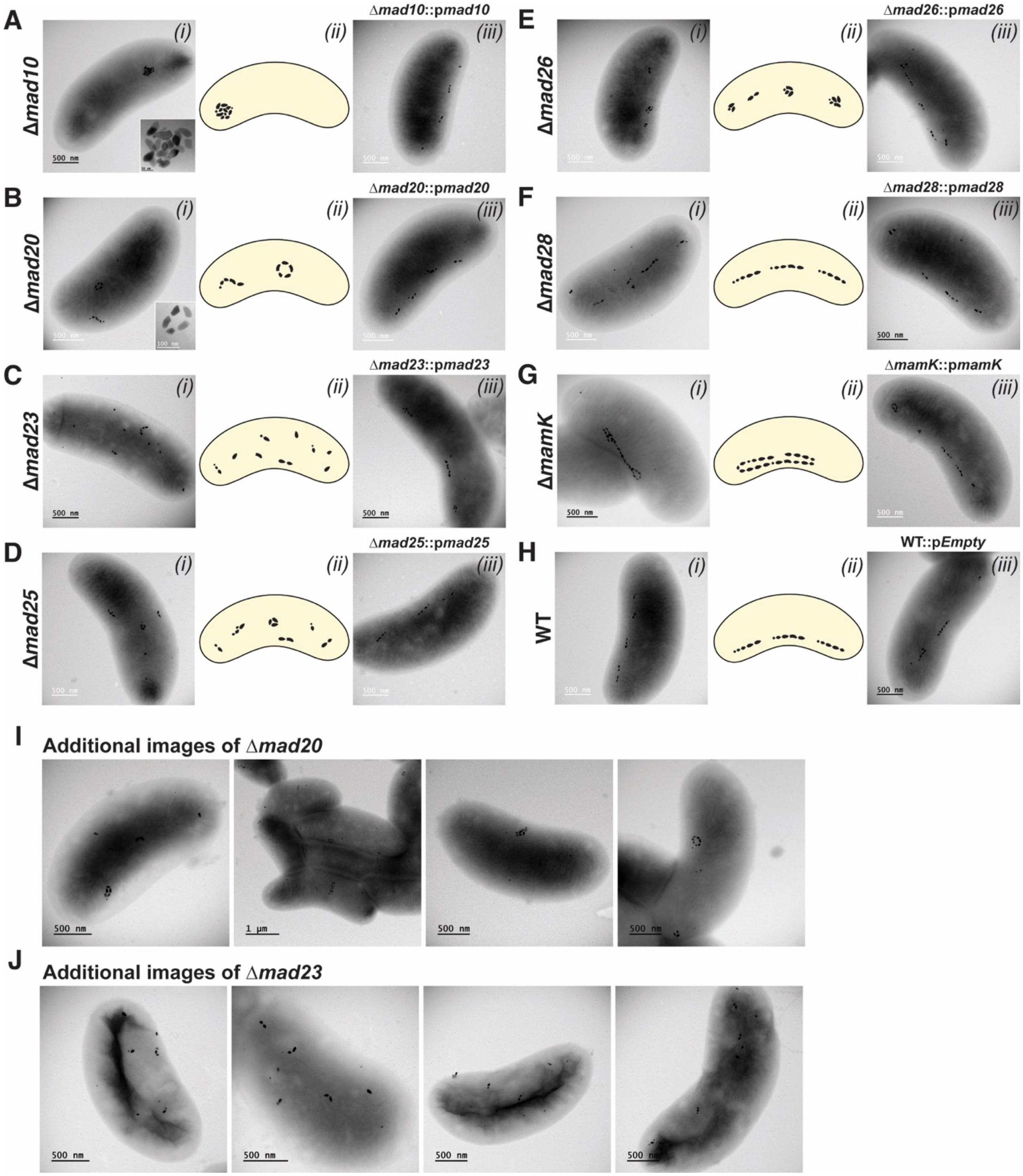

**Supplemental S6.** *TEM images of complementation of deletion mutants*

(A-G) TEM images of deletion mutants and their respective complementation strains in RS-1. All complementations were done by expressing the gene on a plasmid. (H) TEM images of WT and a WT control with an empty plasmid. (I) Additional TEM images of Δ*mad20* in RS-1. These images are to illustrate fewer subchains in each cell and more crystals per subchain in each cell to complement the statistical data from Supplemental Figure S1. Perhaps rings form in this mutant because subchains are too long, similar to the Δ*mamK* phenotype. (J) Additional TEM images of Δ*mad23* in RS-1. These images are to illustrate the higher number of subchains in each cell and fewer crystals per subchain in each cell to complement the statistical data from Supplemental Figure S1. Subchains are more scattered in Δ*mad23*.

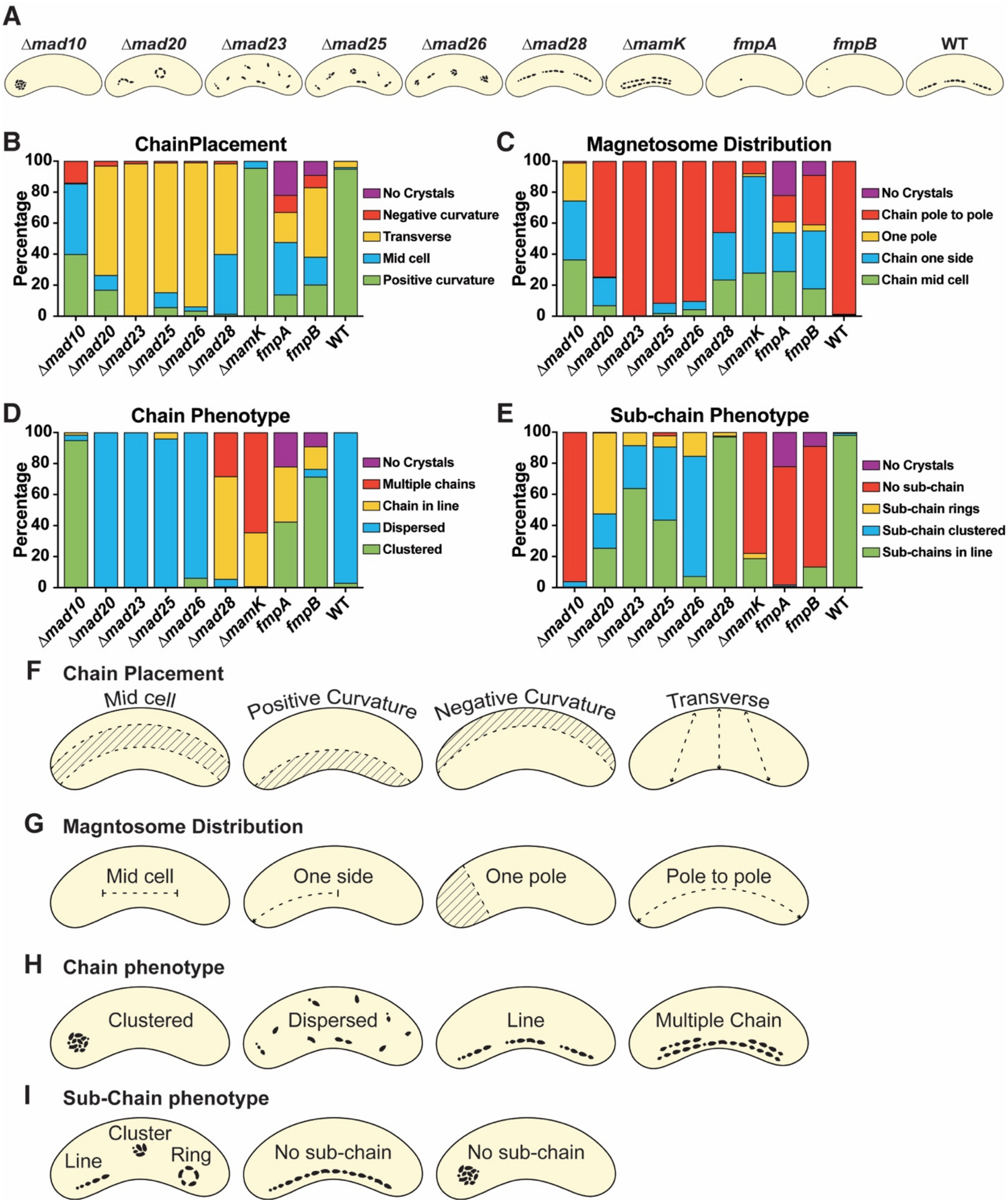

**Supplemental S7.** *Additional mutant phenotypes and magnetosome chain and subchain categories*

(A) Illustrations of the phenotypes of the different mutants in this study. (B-E) Additional phenotype categories for all mutants. (F-I) Categories used to calculate mutant phenotypes in Figure 4, Supplemental Figure S1, as well as (B-E) in this figure.

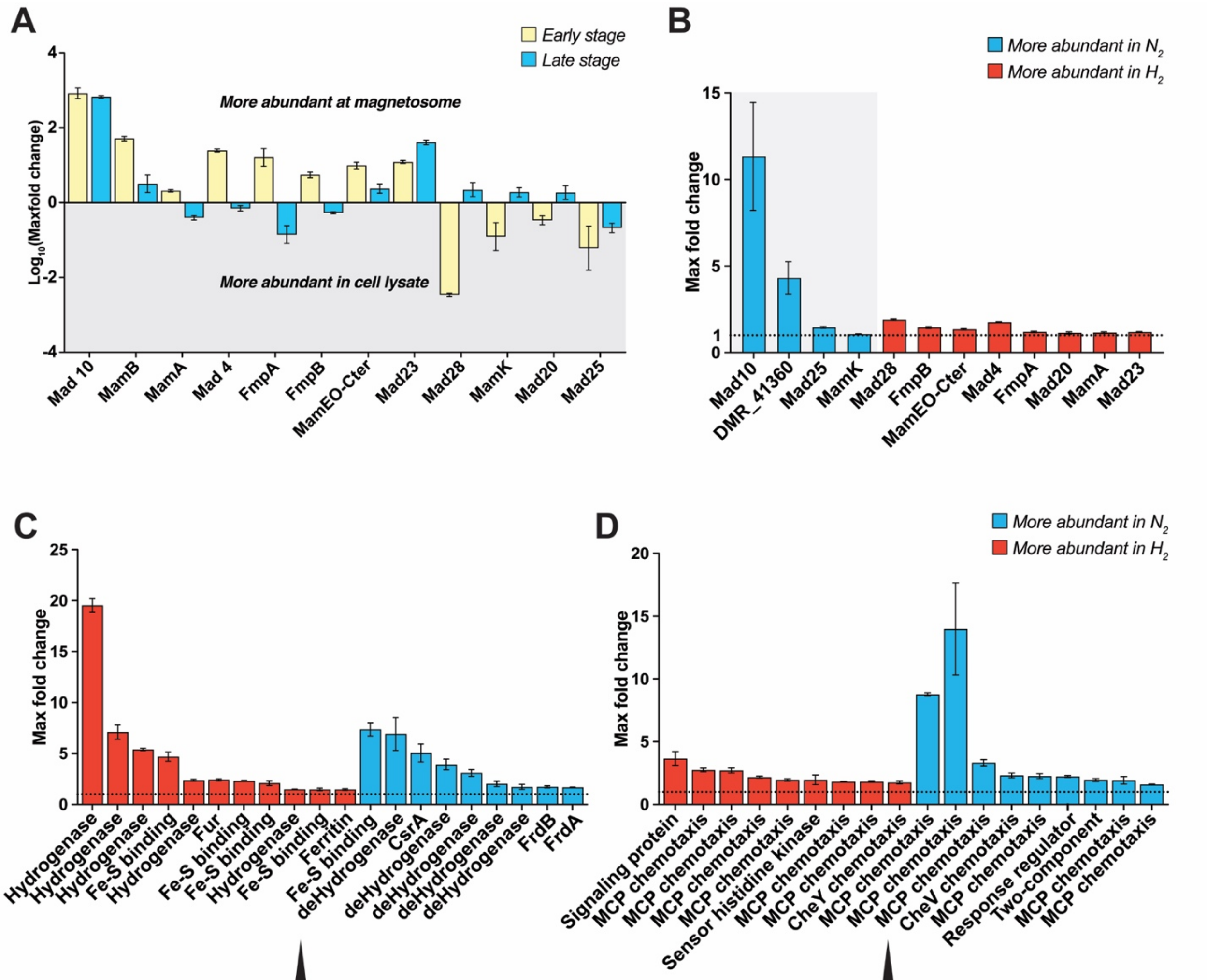

**E**

| | Protein name | Highest |
|---|---|---|
| 1 | DMR 07840 Hydrogenase | Hydrogen |
| 2 | DMR 07830 Hydrogenase | Hydrogen |
| 3 | DMR 07850 Hydrogenase | Hydrogen |
| 4 | DMR 19790 Fur ferric uptake regulation | Hydrogen |
| 5 | DMR 01950 iron-sulfur binding | Hydrogen |
| 6 | DMR 01930 Hydrogenase | Hydrogen |
| 7 | DMR 01940 iron-sulfur binding | Hydrogen |
| 8 | DMR 20050 iron-sulfur binding | Hydrogen |
| 9 | DMR 12950 Hydrogenase | Hydrogen |
| 10 | DMR 17620 ferritin | Hydrogen |
| 11 | DMR 42710 iron-sulfur binding | Hydrogen |
| 12 | DMR 31480 csrA carbon storage regulator | Nitrogen |
| 13 | DMR 42500 iron-sulfur binding | Nitrogen |
| 14 | DMR 01890 deHydrogenase | Nitrogen |
| 15 | DMR 16050 deHydrogenase | Nitrogen |
| 16 | DMR 21490 deHydrogenase | Nitrogen |
| 17 | DMR 05780 frdB fumarate reductase | Nitrogen |
| 18 | DMR 19380 deHydrogenase | Nitrogen |
| 19 | DMR 08200 deHydrogenase | Nitrogen |
| 20 | DMR 34280 frdA fumarate reductase | Nitrogen |

**F**

| | Protein name | Highest |
|---|---|---|
| 1 | DMR_09360 signaling protein | Hydrogen |
| 2 | DMR_28950 methyl-accepting chemotaxis | Hydrogen |
| 3 | DMR_00340 methyl-accepting chemotaxis | Hydrogen |
| 4 | DMR_37860 methyl-accepting chemotaxis | Hydrogen |
| 5 | DMR_27200 methyl-accepting chemotaxis | Hydrogen |
| 6 | DMR_34160 sensor histidine kinase | Hydrogen |
| 7 | DMR_38310 methyl-accepting chemotaxis | Hydrogen |
| 8 | DMR_04320 methyl-accepting chemotaxis | Hydrogen |
| 9 | DMR_23920 CheY chemotaxis | Hydrogen |
| 10 | DMR_26500 methyl-accepting chemotaxis | Nitrogen |
| 11 | DMR_07950 methyl-accepting chemotaxis | Nitrogen |
| 12 | DMR_29030 methyl-accepting chemotaxis | Nitrogen |
| 13 | DMR_26640 CheV chemotaxis | Nitrogen |
| 14 | DMR_07730 methyl-accepting chemotaxis | Nitrogen |
| 15 | DMR_41540 response regulator | Nitrogen |
| 16 | DMR_45100 2-component sensor & regulator | Nitrogen |
| 17 | DMR_08750 methyl-accepting chemotaxis | Nitrogen |
| 18 | DMR_27400 methyl-accepting chemotaxis | Nitrogen |

**Supplemental S8.** *Additional proteomics data.*

(A) Additional proteomic analysis of magnetosome proteins comparing protein abundance in the cell lysate versus the magnetosome fraction. The abundance of magnetosome proteins is represented as greater than 1 when they are more prevalent in the magnetosome fraction and as less than 1 when they are more abundant in the cell lysate. (B) The maximum fold change of magnetosome proteins detected in cell lysates under both nitrogen and hydrogen conditions. Blue bars represent proteins more abundant in nitrogen condition and orange bars represent proteins more abundant in hydrogen condition. (C) and (D) Additional proteomic data comparing protein abundance in nitrogen versus hydrogen conditions, highlighting non-magnetosome proteins with significant maximum fold changes. (E) and (F) display the gene names and locus IDs corresponding to all bars in (C) and (D), respectively.

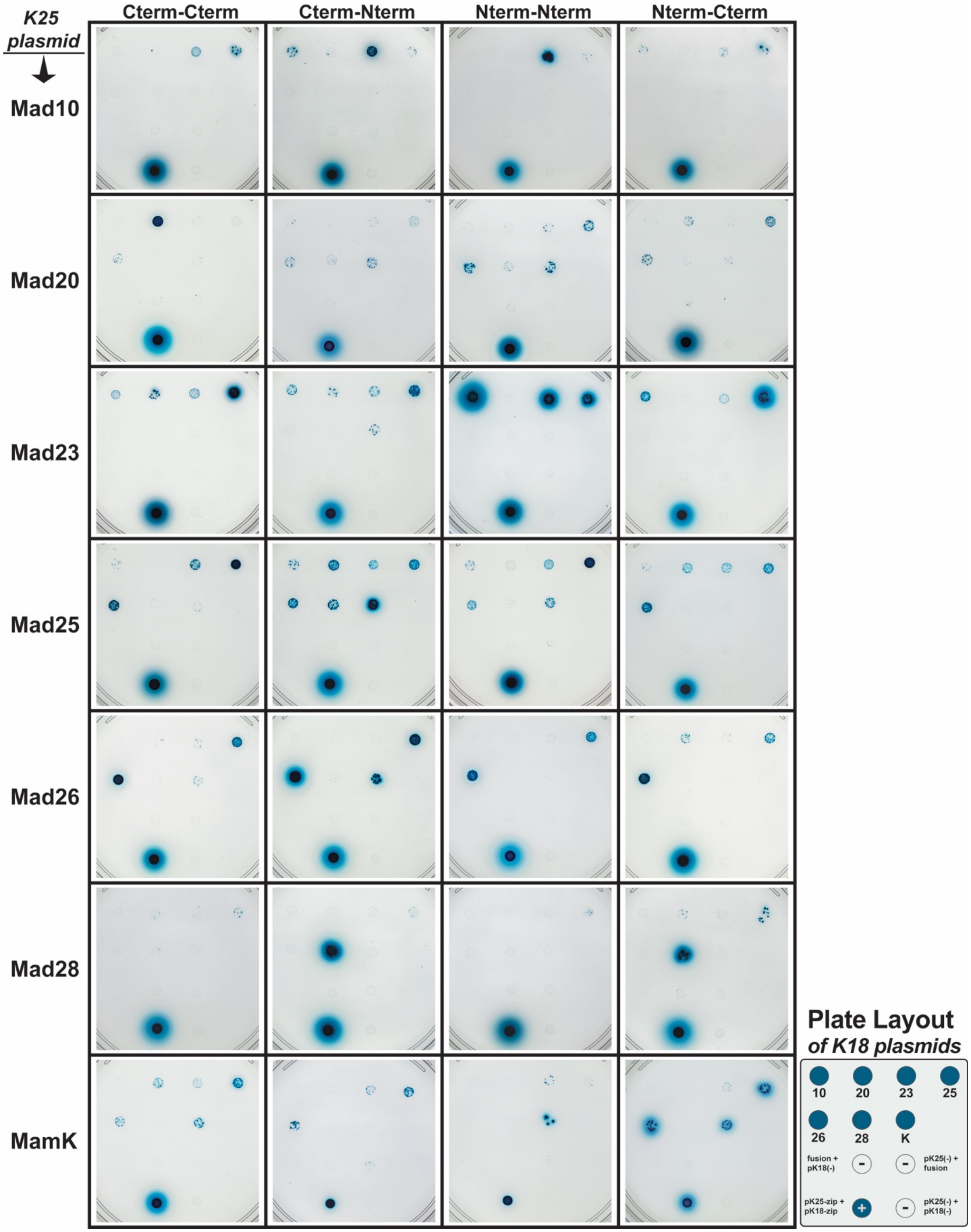

**Supplemental S9.** *BACTH images of plates for all interactions.*

Image of all plates used to construct the table of all of the interactions in Supplemental Figure S2. The illustration on the bottom right shows the layout for each plate which included for controls:

**Extended data Table:**

| **Phyla** | **Organiam** | **16S gene ID** | **Genome ID** | **Shape reference** | **MGC reference** |
|---|---|---|---|---|---|
| *Alpha* | *Magnetospirillum magneticum* AMB-1 | D17514.1 | NCBI:txid342108 | 11 | 12 |
| *Alpha* | *Magnetospirillum magnetotacticum* MS-1 | IMG: 2647169949 | NCBI:txid272627 | 13 | 14 |
| *Alpha* | *Magnetospirillum caucaseum* SO-1 | JX502622.2 | NCBI:txid1244869 | 15 | 15–17 |
| *Alpha* | *Magnetospirillum* ME-1 | IMG: 2676550241 | NCBI:txid1639348 | 18 | 16,17,19 |
| *Alpha* | *Magnetospirillum* XM-1 | KP966105.1 | NCBI:txid1663591 | 20 | 16,21 |
| *Alpha* | *Magnetospirillum marisnigri* SP-1 | KC252630.3 | NCBI:txid1285242 | 15 | 17,22 |
| *Alpha* | *Magnetospirillum kuznetsovii* LBB-42 | NR_180134.1 | NCBI:txid2053833 | 23 | 16,23 |
| *Alpha* | *Magnetospirillum gryphiswaldense* MSR-1 | NR_121771.1 | NCBI:txid431944 | 24,25 | 26 |
| *Alpha* | *Magnetospirillum moscoviense* BB-1 | KF712468.2 | NCBI:txid1437059 | 15 | 17,22 |
| *Alpha* | *Magnetospirillum* sp. LM-5 | IMG: 2894467686 | NCBI:txid2681466 | 27 | 17 |
| *Alpha* | *Magnetospirillum* sp. SS-4 | IMG: 2894461381 | NCBI:txid2681465 | 27 | 17 |
| *Alpha* | *Magnetospirillum* sp. UT-4 | IMG: 2894472958 | NCBI:txid2681467 | 27 | 17 |

| | | | | | |
|---|---|---|---|---|---|
| *Alpha* | *Rhodospirillaceae* LM-1 | JF490044.1 | NCBI:txid1008128 | 27 | 17 |
| *Alpha* | *Magnetospira* QH-2 | EU675666.1 | NCBI:txid1288970 | 28 | 29 |
| *Alpha* | *Ca. Terasakiella magnetica* PR1 | IMG: 2752957094 | NCBI:txid1867952 | 30 | 30 |
| *Alpha* | *Magnetovibrio blakemorei* MV-1 | L06455.1 | NCBI:txid28181 | 31 | 32 |
| *Gamma* | Strain BW-2 | HQ595728.1 | NCBI:txid947515 | 33 | 34 |
| *Gamma* | SHHR-1 | KX344069.1 | NCBI:txid1899433 | 35 | 16 |
| *Gamma* | Strain SS-5 | HQ595729.1 | NCBI:txid947516 | 33 | 36 |
| *Eta* | *Ca. Magnetococcus massalia* MO-1 | EF643520.2 | NCBI:txid451514 | 37 | 38 |
| *Eta* | *Magnetococcus* MC-1 | IMG: 640720050 | NCBI:txid156889 | 39 | 40 |
| *Eta* | *Magnetofaba australis* IT-1 | JX534168.1 | NCBI:txid1434232 | 41 | 41 |
| *Eta* | *Ca. Magnetaquicoccus inordinatus* UR-1 | IMG: 2881921666 | NCBI:txid2496818 | 42 | 42 |
| *Desulfobacterota* | *Ca. Magnetoglobus multicellularis* | IMG: 2559591426 | NCBI:txid890399 | 43,44 | 45 |
| *Desulfobacterota* | *Ca. Magnetananas rongchenensis* RPA | KF925363.1 | NCBI:txid1463558 | 46 | 46 |
| *Desulfobacterota* | *Ca. Magnetomorum* HK-1 | IMG: 2648890082 | NCBI:txid1509431 | 47 | 48 |
| *Desulfobacterota* | *Desulfamplus magnetovallimortis* BW-1 | JN252194.1 | NCBI:txid1073250 | 49 | 50 |
| *Desulfobacterota* | *Desulfovibrio magneticus* RS-1 | NR_074958.1 | NCBI:txid573370 | 51,52 | 53 |

| | | | | | |
|---|---|---|---|---|---|
| *Desulfobacterota* | *Desulfovibrio* FSS-1 | LC311577.1 | NCBI:txid2730080 | 54 | 54 |
| *Desulfobacterota* | *Delta Proteobacterium* FH-1 | JF330268 | NCBI:txid999117 | 50 | 50 |
| *Desulfobacterota* | *Desulfonatronum* ML-1 | HQ595725.1 | NCBI:txid947513 | 55 | 50 |
| *Nitrospirota* | *Ca. Magnetoovum chiemensis* WYHC-5 | OL423397.1 | NCBI:txid1609970 | 56 | 56 |
| *Nitrospirota* | *Ca. Magnetobacterium casensis* MYR-1 | MT703955.1 | NCBI:txid1455061 | 57 | 58 |
| *Nitrospirota* | *Ca. Magnetobacterium bavaricum* TM-1 | X71838.1 | NCBI:txid29290 | 59 | 60 |
| *Nitrospirota* | *Ca. Nitrospirae* YQR-1 | ON340538.1 | | 16 | 16 |
| *Nitrospirota* | *Ca. Magnetomonas plexicatena* LBB-01 | MK632185.1 | CP049016.1 | 61 | 61 |
| *Nitrospirota* | *Ca. Magnetominusculus linsii* LBB-02 | MK632186.1 | | 61 | 61 |
| *Nitrospirota* | *Ca. Nitrospirae* MYC-10 | ON342894.1 | | 16 | 16 |
| *Nitrospirota* | *Ca. Magnetocorallium paracelense* XS-1 | OQ281288.1 | NCBI:txid3021403 | 62 | 62 |
| *Elusimicrobiota* | *Ca. Liberimonas magnetica DUR002* | KY516811 | GCA_020523885.1 | 5 | 5 |
| *Elusimicrobiota* | *Ca. Obscuribacterium magneticum DUR003* | JQ369221 | GCA_020523905.1 | 5 | 5 |
| *OP3* | *Ca. Omnitrophus magneticus* SKK-01 | JN412733.1 | NCBI:txid174292 | 63 | 60 |

**Supplemental Table 1.** *Table of species and reference used for phylogenetic tree construction*

## Supplemental Tables

| Strain | Description | Reference |
|---|---|---|
| AK80 | WT | [64] |
| AK268 | WT, Δ*upp* | [65] |
| AK350 | Δ*mad23*, Δ*upp* | This study |
| AK377 | Δ*mad20*, Δ*upp* | This study |
| AK378 | Δ*mad25*, Δ*upp* | This study |
| AK380 | Δ*mad10*, Δ*upp* | This study |
| AK382 | Δ*mad28*, Δ*upp* | This study |
| AK383 | Δ*mad26*, Δ*upp* | This study |
| AK220 | Δ*mamK* | This study |

**Supplemental Table 2.** *Table of all strains used in this study*

| Plasmid | Description | Backbone | Reference |
|---|---|---|---|
| PAK906 | Complementation backbone with pNTP | | [64] |
| PAK907 | Complementation backbone with pmamA | | [64] |
| pAK914 | Deletion backbone with SacB only | | [64] |
| pAK1127 | Deletion backbone with Upp and SacB | | [65] |
| pAK1452 | mad10 deletion plasmid with Strep | pAK1127 | This study |
| pAK1384 | mad20 deletion plasmid with StrAB | pAK1127 | This study |
| pAK1268 | mad23 deletion with strAB for selection and upp counterselection (pCG116) | pAK1127 | This study |
| pAK1386 | mad25 deletion plasmid with StrAB | pAK1127 | This study |
| pAK1387 | mad26 deletion plasmid with StrAB | pAK1127 | This study |
| pAK1388 | mad28 deletion plasmid with StrAB | pAK1127 | This study |
| pAK966 | mamK deletion plasmid with strAB in pAK914 | pAK914 | This study |
| pAK1481 | pAK906–mad10 Complementation | pAK906 | This study |
| pAK1454 | pAK906–mad20 complementation | pAK906 | This study |
| pAK1507 | pAK906–mad23 complementation | pAK906 | This study |
| pAK1480 | pAK907–mad25 Complementation | pAK907 | This study |
| pAK1488 | pAK907–mad26 Complementation | pAK907 | This study |

| | | | |
|---|---|---|---|
| pAK1518 | pAK907– mad28 Complementation (with alt Start) | pAK907 | This study |
| pAK1489 | pAK906–mamK Complementation | pAK906 | This study |
| pAK318 | pKT25 | | EUROMEDEX |
| pAK319 | pKNT25 | | EUROMEDEX |
| pAK320 | pUT18 | | EUROMEDEX |
| pAK321 | pUT18C | | EUROMEDEX |
| pAK322 | pKT25-zip | | EUROMEDEX |
| pAK323 | pUT18C-zip | | EUROMEDEX |
| pAK1525 | KT25-mad10 | pAK318 | This study |
| pAK1526 | mad10-KNT25 | pAK319 | This study |
| pAK1527 | mad10-UT18 | pAK320 | This study |
| pAK1528 | UT18C-mad10 | pAK321 | This study |
| pAK1529 | KT25-mad20 | pAK318 | This study |
| pAK1530 | mad20-KNT25 | pAK319 | This study |
| pAK1531 | mad20-UT18 | pAK320 | This study |
| pAK1532 | UT18C-mad20 | pAK321 | This study |
| pAK1541 | KT25-mad23 | pAK318 | This study |
| pAK1542 | mad23-KNT25 | pAK319 | This study |
| pAK1543 | mad23-UT18 | pAK320 | This study |
| pAK1544 | UT18C-mad23 | pAK321 | This study |
| pAK1549 | KT25-mad25 | pAK318 | This study |
| pAK1550 | mad25-KNT25 | pAK319 | This study |
| pAK1551 | mad25-UT18 | pAK320 | This study |
| pAK1552 | UT18C-mad25 | pAK321 | This study |
| pAK1553 | KT25-mad26 | pAK318 | This study |
| pAK1554 | mad26-KNT25 | pAK319 | This study |
| pAK1555 | mad26-UT18 | pAK320 | This study |
| pAK1556 | UT18C-mad26 | pAK321 | This study |
| pAK1557 | KT25-mad28 | pAK318 | This study |
| pAK1558 | mad28-KNT25 | pAK319 | This study |
| pAK1559 | mad28-UT18 | pAK320 | This study |
| pAK1560 | UT18C-mad28 | pAK321 | This study |

| | | | |
|---|---|---|---|
| pAK1561 | KT25-mamK | pAK318 | This study |
| pAK1562 | mamK-KNT25 | pAK319 | This study |
| pAK1563 | mamK-UT18 | pAK320 | This study |
| pAK1564 | UT18C-mamK | pAK321 | This study |

**Supplemental Table 3.** *Table of all plasmids used in this study*

All of the plasmids used for this study and the previously published backbones used to generate the plasmids used for this research.

| **Primer** | **Sequence** | **Description** |
|---|---|---|
| VR123-F | AAACGCAAAAGAAAATGCCGATATCCTATTGGCCTCTAGAGGAATTCCAGGATTCCCTCA | mad20 deletion upstream |
| VR124-R | GGATCCCCCATCCACTAAATTTAAATAGGATCCTCTGTCCTTAATCTTGGCC | mad20 deletion upstream |
| VR125-F | GGATCCTATTTAAATTTAGTGGATGGGGGATCCAGGATCGCCAACAATGCCTG | mad20 deletion downstream |
| VR126-R | TGGCGGTCATGGTCTTTTCGGCGAGCTTCTCTAGAAGCTCCGCTTCAAGAACCAC | mad20 deletion downstream |
| VR127-F | AAACGCAAAAGAAAATGCCGATATCCTATTGGCCTCTAGACAAGTGGAGTTAGGGTGATT | mad25 deletion upstream |
| VR128-R | CATATGCCCATCCACTAAATTTAAATACATATGGTCAGCTTTAAAAAGGGCCA | mad25 deletion upstream |
| VR129-F | CATATGTATTTAAATTTAGTGGATGGGCATATGTGTTCGGCCATTGCCGTTAT | mad25 deletion downstream |
| VR130-R | TGGTGGCGGTCATGGTCTTTTCGGCGAGCTTCTCTAGACCTCGTCTCTCTAACACAAA | mad25 deletion downstream |
| VR131-F | AAACGCAAAAGAAAATGCCGATATCCTATTGGCCTCTAGACATCAAAAGCATGGAAGGGC | mad26 deletion upstream |
| VR132-R | GGATCCCCCATCCACTAAATTTAAATAGGATCCTTCGCGCTGCATTCCGTCCA | mad26 deletion upstream |
| VR133-F | GGATCCTATTTAAATTTAGTGGATGGGGGATCCACTATTGCCTTGAATAAATG | mad26 deletion downstream |
| VR134-R | TGGTGGCGGTCATGGTCTTTTCGGCGAGCTTCTCTAGAGCATCCAAGCGTTCTTTTTG | mad26 deletion downstream |

| | | |
|---|---|---|
| VR135-F | AAACGCAAAAGAAAATGCCGATATCCTATTGGCCTCTAGAAACGGTTTACAGCGGATACA | mad28 deletion upstream |
| VR136-R | GGATCCCCCATCCACTAAATTTAAATAGGATCCGCATCCAAGCGTTCTTTTTG | mad28 deletion upstream |
| VR137-F | GGATCCTATTTAAATTTAGTGGATGGGGGATCCGGCCCTGACCGAGGCGGATT | mad28 deletion downstream |
| VR138-R | TGGCGGTCATGGTCTTTTCGGCGAGCTTCTCTAGACAAAATGGAGATTGGAGGAA | mad28 deletion downstream |
| VR147-F | AGGCGGGCATGGCCAAGATTAAGGACAGAGGATCCCTGCTAAAGGAAGCGGAACACG | Add StrAB-mad20-F |
| VR148-R | ATTCGCTATCAGGCATTGTTGGCGATCCTGGATCCCTAGTATGACGTCTGTCGCACCT | Add StrAB-mad20-R |
| VR149-F | AGGGGCCATGGCCCTTTTTAAAGCTGACCATATGCTGCTAAAGGAAGCGGAACACG | Add StrAB-mad25-F |
| VR150-R | GAAAAAGCATAACGGCAATGGCCGAACACATATGCTAGTATGACGTCTGTCGCACCT | Add StrAB-mad25-R |
| VR151-F | GGGCAAACACTCCCGGTCGATTCCGGACAGGATCCCTGCTAAAGGAAGCGGAACACG | Add StrAB-mad26-F |
| VR152-R | ATCACAGTTCATTTATTCAAGGCAATAGTGGATCCCTAGTATGACGTCTGTCGCACCT | Add StrAB-mad26-R |
| VR153-F | ATATTCGAGCAAAAAGAACGCTTGGATGCGGATCCCTGCTAAAGGAAGCGGAACACG | Add StrAB-mad28-F |
| VR154-R | GGTATGGCTAATCCGCCTCGGTCAGGGCCGGATCCCTAGTATGACGTCTGTCGCACCT | Add StrAB-mad28-R |
| VR319-F | GTCATGGTCTTTTCGGCGAGCTTCTCTAGAATCTCCAAAAAGTTGCTGGGC | mad10 deletion upstream |
| VR320-R | CCCATCCACTAAATTTAAATAGGATCCTCTTCCATGGCGTCCTCCG | mad10 deletion upstream |
| VR321-F | TATTTAAATTTAGTGGATGGGGGATCCCCAGTGCGCAGCCGGCCTGA | mad10 deletion downstream |
| VR322-R | GAAAATGCCGATATCCTATTGGCCTCTAGATCGCGGCCTGGGCC | mad10 deletion downstream |

| | | |
|---|---|---|
| VR323-F | CGACAATGCGCGGAGGACGCCATGGAAGAGCTGCTAAAGGAAGCGGAACAC | Add StrAB-mad10-F |
| VR324-R | GAGATGATCTCAGGCCGGCTGCGCACTGGGCTAGTATGACGTCTGTCGCACC | Add StrAB-mad10-R |
| VR277-F | AGACAGGATGAGGATCGTTTCGCGTCGACTGATCATCTCCCGGCGGG | mad20 complementation in pAK906 |
| VR278-R | GGGAATTCGAGCTCGGTACCCGGGGATCCTGCGCCGCTCCTGGATTC | mad20 complementation in pAK906 |
| CG220-R | GAGCTCGGTACCCGGGGATCCTCTAGAACTTGCTTTTCCGCCGTCATAC | mad23 complementation in pAK906 |
| CG221-F | CAAGAGACAGGATGAGGATCGTTTCGCGATGGAAGACGCCATGAGCTC | mad23 complementation in pAK906 |
| VR335-F | AAGCCAAGAAAAACGTCGCCAACGTCGACTATGGCCCTTTTTAAAGCTGACG | mad25 complementation in pAK907 |
| VR336-R | GGGAATTCGAGCTCGGTACCCGGGGATCCTCTACCCGTCTGCGACGTC | mad25 complementation in pAK907 |
| VR337-F | AGACAGGATGAGGATCGTTTCGCGTCGACTATGGAAGAAAATACCCGCTACA | mad10 complementation in pAK906 |
| VR338R | GGGAATTCGAGCTCGGTACCCGGGGATCCTTCAGGCCGGCTGCG | mad10 complementation in pAK906 |
| VR355-F | AAGCCAAGAAAAACGTCGCCAACGTCGACTATGGACGGAATGCAGCGC | mad26 complementation in pAK907 |

| | | |
|---|---|---|
| VR356-R | GGGAATTCGAGCTCGGTACCCGGGGATCCTTCATTTATTCAAGGCAATAGTCAGT | mad26 complementation in pAK907 |
| VR357-F | AGACAGGATGAGGATCGTTTCGCGTCGACTATGTCCGGAAGCAACGTGC | mamK complementation in pAK906 |
| VR358-R | GGGAATTCGAGCTCGGTACCCGGGGATCCTTTAATCCTTTCGCAGCTCGTC | mamK complementation in pAK906 |
| VR375-F | AAGCCAAGAAAAACGTCGCCAACGTCGACTACAGCTCTGGCGCTCTTG | mad28 complementation in pAK907 (with pmad28 & alt-start) |
| VR372-R | GGGAATTCGAGCTCGGTACCCGGGGATCCTCTAATCCGCCTCGGTCAGG | mad28 complementation in pAK907 (with pmad28 & alt-start) |
| VR390-F | CGGGCTGCAGGGTCGACTCTAGAGGATCCCATGGAAGAAAATACCCGCTACA | KT25_mad10 |
| VR391-R | TCACGACGTTGTAAAACGACGGCCGAATTCTCAGGCCGGCTGCG | KT25_mad10 |
| VR392-F | ACAGCTATGACCATGATTACGCCAAGCTTGATGGAAGAAAATACCCGCTACA | KNT25_mad10-noStop |
| VR393-R | CCGGGGATCCTCTAGAGTCGACCTGCAGGCGGCCGGCTGCGCA | KNT25_mad10-noStop |
| VR394-F | ACAGCTATGACCATGATTACGCCAAGCTTGATGGAAGAAAATACCCGCTACA | UT18_mad10-NoStop |
| VR395-R | CCGGGGATCCTCTAGAGTCGACCTGCAGGCGGCCGGCTGCGCA | UT18_mad10-NoStop |
| VR396-F | CGCCACTGCAGGTCGACTCTAGAGGATCCCATGGAAGAAAATACCCGCTACA | UT18C_mad10 |
| VR397-R | TAGTTATATCGATGAATTCGAGCTCGGTACTCAGGCCGGCTGCG | UT18C_mad10 |
| VR398-F | CGGGCTGCAGGGTCGACTCTAGAGGATCCCATGGCCAAGATTAAGGACAGACT | KT25_mad20 |

| | | |
|---|---|---|
| VR399-R | TCACGACGTTGTAAAACGACGGCCGAATTCTCAGGCATTGTTGGCGATCC | KT25_mad20 |
| VR400-F | ACAGCTATGACCATGATTACGCCAAGCTTGATGGCCAAGATTAAGGACAGACT | KNT25_mad20-noStop |
| VR401-R | CCGGGGATCCTCTAGAGTCGACCTGCAGGCGGCATTGTTGGCGATCCTCT | KNT25_mad20-noStop |
| VR402-F | ACAGCTATGACCATGATTACGCCAAGCTTGATGGCCAAGATTAAGGACAGACT | UT18_mad20-NoStop |
| VR403-R | CCGGGGATCCTCTAGAGTCGACCTGCAGGCGGCATTGTTGGCGATCCTCT | UT18_mad20-NoStop |
| VR404-F | CGCCACTGCAGGTCGACTCTAGAGGATCCCATGGCCAAGATTAAGGACAGACT | UT18C_mad20 |
| VR405-R | TAGTTATATCGATGAATTCGAGCTCGGTACTCAGGCATTGTTGGCGATCC | UT18C_mad20 |
| VR422-F | CGGGCTGCAGGGTCGACTCTAGAGGATCCCATGGAAGACGCCATGAGCTC | KT25_mad23 |
| VR423-R | TCACGACGTTGTAAAACGACGGCCGAATTCCTAACTCCACTTGTAGCGCA | KT25_mad23 |
| VR424-F | ACAGCTATGACCATGATTACGCCAAGCTTGATGGAAGACGCCATGAGCTC | KNT25_mad23-noStop |
| VR425-R | CCGGGGATCCTCTAGAGTCGACCTGCAGGCACTCCACTTGTAGCGCATGC | KNT25_mad23-noStop |
| VR426-F | ACAGCTATGACCATGATTACGCCAAGCTTGATGGAAGACGCCATGAGCTC | UT18_mad23-NoStop |
| VR427-R | CCGGGGATCCTCTAGAGTCGACCTGCAGGCACTCCACTTGTAGCGCATGC | UT18_mad23-NoStop |
| VR428-F | CGCCACTGCAGGTCGACTCTAGAGGATCCCATGGAAGACGCCATGAGCTC | UT18C_mad23 |
| VR429-R | TAGTTATATCGATGAATTCGAGCTCGGTACCTAACTCCACTTGTAGCGCA | UT18C_mad23 |
| VR438-F | CGGGCTGCAGGGTCGACTCTAGAGGATCCCATGGCCCTTTTTAAAGCTGACG | KT25_mad25 |

| | | |
|---|---|---|
| VR439-R | TCACGACGTTGTAAAACGACGGCCGAATTCCTACCCGTCTGCGACGTC | KT25_mad25 |
| VR440-F | ACAGCTATGACCATGATTACGCCAAGCTTGATGGCCCTTTTTAAAGCTGACG | KNT25_mad25-noStop |
| VR441-R | CCGGGGATCCTCTAGAGTCGACCTGCAGGCCCCGTCTGCGACGTCG | KNT25_mad25-noStop |
| VR442-F | ACAGCTATGACCATGATTACGCCAAGCTTGATGGCCCTTTTTAAAGCTGACG | UT18_mad25-NoStop |
| VR443-R | CCGGGGATCCTCTAGAGTCGACCTGCAGGCCCCGTCTGCGACGTCG | UT18_mad25-NoStop |
| VR444-F | CGCCACTGCAGGTCGACTCTAGAGGATCCCATGGCCCTTTTTAAAGCTGACG | UT18C_mad25 |
| VR445-R | TAGTTATATCGATGAATTCGAGCTCGGTACCTACCCGTCTGCGACGTC | UT18C_mad25 |
| VR446-F | CGGGCTGCAGGGTCGACTCTAGAGGATCCCATGGACGGAATGCAGCGC | KT25_mad26 |
| VR447-R | TCACGACGTTGTAAAACGACGGCCGAATTCTCATTTATTCAAGGCAATAGTCAGT | KT25_mad26 |
| VR448-F | ACAGCTATGACCATGATTACGCCAAGCTTGATGGACGGAATGCAGCGC | KNT25_mad26-noStop |
| VR449-R | CCGGGGATCCTCTAGAGTCGACCTGCAGGCTTTATTCAAGGCAATAGTCAGTTCA | KNT25_mad26-noStop |
| VR450-F | ACAGCTATGACCATGATTACGCCAAGCTTGATGGACGGAATGCAGCGC | UT18_mad26-NoStop |
| VR451-R | CCGGGGATCCTCTAGAGTCGACCTGCAGGCTTTATTCAAGGCAATAGTCAGTTCA | UT18_mad26-NoStop |
| VR452-F | CGCCACTGCAGGTCGACTCTAGAGGATCCCATGGACGGAATGCAGCGC | UT18C_mad26 |
| VR453-R | TAGTTATATCGATGAATTCGAGCTCGGTACTCATTTATTCAAGGCAATAGTCAGT | UT18C_mad26 |
| VR454-F | CGGGCTGCAGGGTCGACTCTAGAGGATCCCATGTCCCAAGAGGATAAGGCG | KT25_mad28 |

| | | |
|---|---|---|
| VR455-R | TCACGACGTTGTAAAACGACGGCCGAATTCCTAATCCGCCTCGGTCAGG | KT25_mad28 |
| VR456-F | ACAGCTATGACCATGATTACGCCAAGCTTGATGTCCCAAGAGGATAAGGCG | KNT25_mad28-noStop |
| VR457-R | CCGGGGATCCTCTAGAGTCGACCTGCAGGCATCCGCCTCGGTCAGGG | KNT25_mad28-noStop |
| VR458-F | ACAGCTATGACCATGATTACGCCAAGCTTGATGTCCCAAGAGGATAAGGCG | UT18_mad28-NoStop |
| VR459-R | CCGGGGATCCTCTAGAGTCGACCTGCAGGCATCCGCCTCGGTCAGGG | UT18_mad28-NoStop |
| VR460-F | CGCCACTGCAGGTCGACTCTAGAGGATCCCATGTCCCAAGAGGATAAGGCG | UT18C_mad28 |
| VR461-R | TAGTTATATCGATGAATTCGAGCTCGGTACCTAATCCGCCTCGGTCAGG | UT18C_mad28 |
| VR462-F | CGGGCTGCAGGGTCGACTCTAGAGGATCCCATGTCCGGAAGCAACGTGC | KT25_mamK |
| VR463-R | TCACGACGTTGTAAAACGACGGCCGAATTCTTAATCCTTTCGCAGCTCGTC | KT25_mamK |
| VR464-F | ACAGCTATGACCATGATTACGCCAAGCTTGATGTCCGGAAGCAACGTGC | KNT25_mamK-noStop |
| VR465-R | CCGGGGATCCTCTAGAGTCGACCTGCAGGCATCCTTTCGCAGCTCGTCC | KNT25_mamK-noStop |
| VR466-F | ACAGCTATGACCATGATTACGCCAAGCTTGATGTCCGGAAGCAACGTGC | UT18_mamK-NoStop |
| VR467-R | CCGGGGATCCTCTAGAGTCGACCTGCAGGCATCCTTTCGCAGCTCGTCC | UT18_mamK-NoStop |
| VR468-F | CGCCACTGCAGGTCGACTCTAGAGGATCCCATGTCCGGAAGCAACGTGC | UT18C_mamK |
| VR469-R | TAGTTATATCGATGAATTCGAGCTCGGTACTTAATCCTTTCGCAGCTCGTC | UT18C_mamK |

**Supplemental Table 4.** *Table of all primers used in this study*

| | | **Compared with:** | **Mann-Whitney U test** | | **Welch's T-Test** | |
|---|---|---|---|---|---|---|
| **Figure** | **Strain/ Condition** | **Strain/ Condition** | **pValue** | **Significance** | **pValue** | **Significance** |
| Figure 3C | Early | Late | <0.0001 | **** | <0.0001 | **** |
| Figure 3D | Early | Late | <0.0001 | **** | <0.0001 | **** |
| Figure 3E | Early | Late | <0.0001 | **** | <0.0001 | **** |
| Figure 3I | Immature crystals | Mature crystals | --- | --- | 0.0006 | *** |

**Supplemental Table 5.** *Table of all statistical tests used for figure 3 in this study*

| | | **Compared with:** | **One way ANOVA test** | | **Mann-Whitney U test** | |
|---|---|---|---|---|---|---|
| **Figure** | **Strain/ Condition** | **Strain/ Condition** | **pValue** | **Significance** | **pValue** | **Significance** |
| Figure 4D | *fmpA* | WT | <0.0001 | **** | <0.0001 | **** |
| Figure 4D | *fmpB* | WT | <0.0001 | **** | <0.0001 | **** |
| Figure 4E | *fmpA* | WT | <0.0001 | **** | <0.0001 | **** |
| Figure 4E | *fmpB* | WT | <0.0001 | **** | <0.0001 | **** |
| Figure 4F | *fmpA* | WT | <0.0001 | **** | <0.0001 | **** |
| Figure 4F | *fmpB* | WT | <0.0001 | **** | <0.0001 | **** |

**Supplemental Table 6.** *Table of all statistical tests used for Figure 4 in this study*

| | | **Compared with:** | **One way ANOVA test** | | **Mann-Whitney U test** | |
|---|---|---|---|---|---|---|
| **Figure** | **Strain/ Condition** | **Strain/ Condition** | **pValue** | **Significance** | **pValue** | **Significance** |
| Figure 5N*i* | Δ*mamK* | WT | <0.0001 | **** | <0.0001 | **** |
| Figure 5N*i* | Δ*mad28* | WT | 0.9378 | ns | 0.4697 | ns |
| Figure 5N*ii* | Δ*mamK* | WT | <0.0001 | **** | <0.0001 | **** |

| | | | | | | |
|---|---|---|---|---|---|---|
| Figure 5N*ii* | Δ*mad28* | WT | 0.0703 | ns | 0.0053 | ** |

**Supplemental Table 7.** *Table of all statistical tests used for figure 5 in this study*

| | | **Compared with:** | **One way ANOVA test** | | **Mann-Whitney U test** | |
|---|---|---|---|---|---|---|
| **Supplemental Figure** | **Strain/ Condition** | **Strain/ Condition** | **pValue** | **Significance** | **pValue** | **Significance** |
| Figure S1D | Δ*mad10* | WT | 0.1364 | ns | 0.0005 | *** |
| Figure S1D | Δ*mad20* | WT | 0.7606 | ns | 0.3754 | ns |
| Figure S1D | Δ*mad23* | WT | 0.7606 | ns | 0.5328 | ns |
| Figure S1D | Δ*mad25* | WT | 0.3521 | ns | 0.0147 | * |
| Figure S1D | Δ*mad26* | WT | 0.4881 | ns | 0.111 | ns |
| Figure S1D | Δ*mad28* | WT | 0.7606 | ns | 0.3365 | ns |
| Figure S1D | Δ*mamK* | WT | <0.0001 | **** | <0.0001 | **** |

| | | **Compared with:** | **One way ANOVA test** | |
|---|---|---|---|---|
| **Supplemental Figure** | **Strain/Condition** | **Strain/Condition** | **pValue** | **Significance** |
| Figure S1E | Δ*mad10* | WT | <0.0001 | **** |
| Figure S1E | Δ*mad20* | WT | 0.0001 | *** |
| Figure S1E | Δ*mad23* | WT | 0.5127 | ns |
| Figure S1E | Δ*mad25* | WT | 0.9895 | ns |
| Figure S1E | Δ*mad26* | WT | 0.0953 | ns |
| Figure S1E | Δ*mad28* | WT | 0.0381 | * |
| Figure S1E | Δ*mamK* | WT | <0.0001 | **** |

| | | **Compared with:** | **Kruskal-Wallis test** | |
|---|---|---|---|---|
| **Supplemental Figure** | **Strain/Condition** | **Strain/Condition** | **pValue** | **Significance** |
| Figure S1F | Δ*mad10* | WT | <0.0001 | **** |
| Figure S1F | Δ*mad20* | WT | <0.0001 | **** |
| Figure S1F | Δ*mad23* | WT | 0.2744 | ns |

| | | | | |
|---|---|---|---|---|
| Figure S1F | Δ*mad25* | WT | 0.0073 | ** |
| Figure S1F | Δ*mad26* | WT | 0.0805 | ns |
| Figure S1F | Δ*mad28* | WT | 0.0007 | *** |
| Figure S1F | Δ*mamK* | WT | <0.0001 | **** |

**Supplemental Table 8.** *Tables of all statistical tests used for Supplemental Figure S1 in this study*

## References:

1. Liu, Y., Van Den Ent, F. & Löwe, J. Filament structure and subcellular organization of the bacterial intermediate filament–like protein crescentin. *Proc. Natl. Acad. Sci. U.S.A.* **121**, e2309984121 (2024).
2. Pohl, A. *et al.* Decoding Biomineralization: Interaction of a Mad10-Derived Peptide with Magnetite Thin Films. *Nano Lett.* **19**, 8207–8215 (2019).
3. Paysan-Lafosse, T. *et al.* InterPro in 2022. *Nucleic Acids Research* **51**, D418–D427 (2023).
4. Kearse, M. *et al.* Geneious Basic: An integrated and extendable desktop software platform for the organization and analysis of sequence data. *Bioinformatics* **28**, 1647–1649 (2012).
5. Uzun, M. *et al.* Recovery and genome reconstruction of novel magnetotactic Elusimicrobiota from bog soil. *The ISME Journal* **17**, 204–214 (2023).
6. Gilchrist, C. L. M. & Chooi, Y.-H. clinker & clustermap.js: automatic generation of gene cluster comparison figures. *Bioinformatics* **37**, 2473–2475 (2021).
7. Hallgren, J. *et al.* DeepTMHMM predicts alpha and beta transmembrane proteins using deep neural networks. Preprint at https://doi.org/10.1101/2022.04.08.487609 (2022).
8. Ludwiczak, J., Winski, A., Szczepaniak, K., Alva, V. & Dunin-Horkawicz, S. DeepCoil—a fast and accurate prediction of coiled-coil domains in protein sequences. *Bioinformatics* **35**, 2790–2795 (2019).
9. Mirdita, M. *et al.* ColabFold: making protein folding accessible to all. *Nat Methods* **19**, 679–682 (2022).
10. Meng, E. C. *et al.* UCSF ChimeraX: Tools for structure building and analysis. *Protein Sci* **32**, e4792 (2023).
11. Li, J. & Pan, Y. Environmental Factors Affect Magnetite Magnetosome Synthesis in Magnetospirillum magneticum AMB-1: Implications for Biologically Controlled Mineralization. *Geomicrobiology Journal* **29**, 362–373 (2012).

12. Matsunaga, T. *et al.* Complete genome sequence of the facultative anaerobic magnetotactic bacterium Magnetospirillum sp. strain AMB-1. *DNA Res* **12**, 157–166 (2005).
13. Maratea, D. & Blakemore, R. P. Aquaspirillum magnetotacticum sp. nov., a Magnetic Spirillum. *International Journal of Systematic and Evolutionary Microbiology* **31**, 452–455 (1981).
14. Smalley, M. D., Marinov, G. K., Bertani, L. E. & DeSalvo, G. Genome Sequence of Magnetospirillum magnetotacticum Strain MS-1. *Genome Announc* **3**, e00233-15 (2015).
15. Dziuba, M. *et al.* Magnetospirillum caucaseum sp. nov., Magnetospirillum marisnigri sp. nov. and Magnetospirillum moscoviense sp. nov., freshwater magnetotactic bacteria isolated from three distinct geographical locations in European Russia. *International Journal of Systematic and Evolutionary Microbiology* **66**, 2069–2077 (2016).
16. Liu, P. *et al.* Key gene networks that control magnetosome biomineralization in magnetotactic bacteria. *National Science Review* **10**, nwac238 (2023).
17. Monteil, C. L. *et al.* Repeated horizontal gene transfers triggered parallel evolution of magnetotaxis in two evolutionary divergent lineages of magnetotactic bacteria. *The ISME Journal* **14**, 1783–1794 (2020).
18. Ke, L. *et al.* Characteristics and optimised fermentation of a novel magnetotactic bacterium, Magnetospirillum sp. ME-1. *FEMS Microbiology Letters* **365**, fny052 (2018).
19. Ke, L., Liu, P., Liu, S. & Gao, M. Complete Genome Sequence of Magnetospirillum sp. ME-1, a Novel Magnetotactic Bacterium Isolated from East Lake, Wuhan, China. *Genome Announc* **5**, e00485-17 (2017).
20. Wang, Y. *et al.* Characterizing and optimizing magnetosome production of Magnetospirillum sp. XM-1 isolated from Xi’an City Moat, China. *FEMS Microbiology Letters* **362**, fnv167 (2015).
21. Wang, Y. *et al.* Complete Genome Sequence of Magnetospirillum sp. Strain XM-1, Isolated from the Xi’an City Moat, China. *Genome Announc* **4**, e01171-16 (2016).

22. Koziaeva, V. V. *et al.* Draft Genome Sequences of Two Magnetotactic Bacteria, Magnetospirillum moscoviense BB-1 and Magnetospirillum marisnigri SP-1. *Genome Announc* **4**, e00814-16 (2016).
23. Koziaeva, V. V. *et al.* Magnetospirillum kuznetsovii sp. nov., a novel magnetotactic bacterium isolated from a lake in the Moscow region. *International Journal of Systematic and Evolutionary Microbiology* **69**, 1953–1959 (2019).
24. Fdez-Gubieda, M. L. *et al.* Magnetite Biomineralization in Magnetospirillum gryphiswaldense: Time-Resolved Magnetic and Structural Studies. *ACS Nano* **7**, 3297–3305 (2013).
25. Schleifer, K. H. *et al.* The Genus *Magnetospirillum* gen. nov. Description of *Magnetospirillum gryphiswaldense* sp. nov. and Transfer of *Aquaspirillum magnetotacticum* to *Magnetospirillum magnetotacticum* comb. nov. *Systematic and Applied Microbiology* **14**, 379–385 (1991).
26. Wang, X. *et al.* Complete Genome Sequence of Magnetospirillum gryphiswaldense MSR-1. *Genome Announc* **2**, e00171-14 (2014).
27. Lefèvre, C. T. *et al.* Insight into the Evolution of Magnetotaxis in Magnetospirillum spp., Based on *mam* Gene Phylogeny. *Appl Environ Microbiol* **78**, 7238–7248 (2012).
28. Zhu, K. *et al.* Isolation and characterization of a marine magnetotactic spirillum axenic culture QH-2 from an intertidal zone of the China Sea. *Research in Microbiology* **161**, 276–283 (2010).
29. Ji, B. *et al.* Comparative genomic analysis provides insights into the evolution and niche adaptation of marine Magnetospira sp. QH-2 strain. *Environmental Microbiology* **16**, 525–544 (2014).
30. Monteil, C. L. *et al.* Genomic study of a novel magnetotactic Alphaproteobacteria uncovers the multiple ancestry of magnetotaxis. *Environmental Microbiology* **20**, 4415–4430 (2018).
31. Bazylinski, D. A. *et al.* Magnetovibrio blakemorei gen. nov., sp. nov., a magnetotactic bacterium (Alphaproteobacteria: Rhodospirillaceae) isolated from a salt marsh. *International Journal of Systematic and Evolutionary Microbiology* **63**, 1824–1833 (2013).

32. Trubitsyn, D. *et al.* Draft Genome Sequence of Magnetovibrio blakemorei Strain MV-1, a Marine Vibrioid Magnetotactic Bacterium. *Genome Announc* **4**, e01330-16 (2016).
33. Lefèvre, C. T. *et al.* Novel magnetite-producing magnetotactic bacteria belonging to the Gammaproteobacteria. *ISME J* **6**, 440–450 (2012).
34. Geurink, C. *et al.* Complete Genome Sequence of Strain BW-2, a Magnetotactic Gammaproteobacterium in the Family Ectothiorhodospiraceae, Isolated from a Brackish Spring in Death Valley, California. *Microbiol Resour Announc* **9**, e01144-19 (2020).
35. Li, J. *et al.* Single-Cell Resolution of Uncultured Magnetotactic Bacteria via Fluorescence-Coupled Electron Microscopy. *Appl Environ Microbiol* **83**, e00409-17 (2017).
36. Trubitsyn, D. *et al.* Complete Genome Sequence of Strain SS-5, a Magnetotactic Gammaproteobacterium Isolated from the Salton Sea, a Shallow, Saline, Endorheic Rift Lake Located on the San Andreas Fault in California. *Microbiol Resour Announc* **10**, e00928-20 (2021).
37. Lefèvre, C. T., Bernadac, A., Yu-Zhang, K., Pradel, N. & Wu, L.-F. Isolation and characterization of a magnetotactic bacterial culture from the Mediterranean Sea. *Environmental Microbiology* **11**, 1646–1657 (2009).
38. Ji, B. *et al.* The chimeric nature of the genomes of marine magnetotactic coccoid-ovoid bacteria defines a novel group of Proteobacteria. *Environmental Microbiology* **19**, 1103–1119 (2017).
39. Meldrum, F. C., Mann, S., Heywood, B. R., Frankel, R. B. & Bazylinski, D. A. Electron microscopy study of magnetosomes in a cultured coccoid magnetotactic bacterium. *Proceedings of the Royal Society of London. Series B: Biological Sciences* **251**, 231–236 (1993).
40. Schübbe, S. *et al.* Complete Genome Sequence of the Chemolithoautotrophic Marine Magnetotactic Coccus Strain MC-1. *Appl Environ Microbiol* **75**, 4835–4852 (2009).

41. Morillo, V. *et al.* Isolation, cultivation and genomic analysis of magnetosome biomineralization genes of a new genus of South-seeking magnetotactic cocci within the Alphaproteobacteria. *Frontiers in Microbiology* **5**, (2014).
42. Koziaeva, V. *et al.* Genome-Based Metabolic Reconstruction of a Novel Uncultivated Freshwater Magnetotactic coccus “Ca. Magnetaquicoccus inordinatus” UR-1, and Proposal of a Candidate Family “Ca. Magnetaquicoccaceae”. *Frontiers in Microbiology* **10**, (2019).
43. Abreu, F. *et al.* Cell Adhesion, Multicellular Morphology, and Magnetosome Distribution in the Multicellular Magnetotactic Prokaryote Candidatus Magnetoglobus multicellularis. *Microscopy and Microanalysis* **19**, 535–543 (2013).
44. Abreu, F. *et al.* ‘Candidatus Magnetoglobus multicellularis’, a multicellular, magnetotactic prokaryote from a hypersaline environment. *International Journal of Systematic and Evolutionary Microbiology* **57**, 1318–1322 (2007).
45. Abreu, F. *et al.* Deciphering unusual uncultured magnetotactic multicellular prokaryotes through genomics. *The ISME Journal* **8**, 1055–1068 (2014).
46. Leão, P. *et al.* Ultrastructure of ellipsoidal magnetotactic multicellular prokaryotes depicts their complex assemblage and cellular polarity in the context of magnetotaxis. *Environmental Microbiology* **19**, 2151–2163 (2017).
47. Zhang, R. *et al.* Characterization and phylogenetic identification of a species of spherical multicellular magnetotactic prokaryotes that produces both magnetite and greigite crystals. *Research in Microbiology* **165**, 481–489 (2014).
48. Kolinko, S., Richter, M., Glöckner, F.-O., Brachmann, A. & Schüler, D. Single-cell genomics reveals potential for magnetite and greigite biomineralization in an uncultivated multicellular magnetotactic prokaryote. *Environmental Microbiology Reports* **6**, 524–531 (2014).
49. Lefèvre, C. T. *et al.* A Cultured Greigite-Producing Magnetotactic Bacterium in a Novel Group of Sulfate-Reducing Bacteria. *Science* **334**, 1720–1723 (2011).
50. Lefèvre, C. T. *et al.* Comparative genomic analysis of magnetotactic bacteria from the Deltaproteobacteria provides new insights into magnetite and greigite magnetosome genes required for magnetotaxis. *Environmental Microbiology* **15**, 2712–2735 (2013).

51. Sakaguchi, T., Burgess, J. G. & Matsunaga, T. Magnetite formation by a sulphate-reducing bacterium. *Nature* **365**, 47–49 (1993).
52. Sakaguchi, T., Arakaki, A. & Matsunaga, T. Desulfovibrio magneticus sp. nov., a novel sulfate-reducing bacterium that produces intracellular single-domain-sized magnetite particles. *International Journal of Systematic and Evolutionary Microbiology* **52**, 215–221 (2002).
53. Nakazawa, H. *et al.* Whole genome sequence of *Desulfovibrio magneticus* strain RS-1 revealed common gene clusters in magnetotactic bacteria. *Genome Res.* **19**, 1801–1808 (2009).
54. Shimoshige, H. *et al.* Isolation and cultivation of a novel sulfate-reducing magnetotactic bacterium belonging to the genus Desulfovibrio. *PLoS ONE* **16**, e0248313 (2021).
55. Lefèvre, C. T., Frankel, R. B., Pósfai, M., Prozorov, T. & Bazylinski, D. A. Isolation of obligately alkaliphilic magnetotactic bacteria from extremely alkaline environments. *Environmental Microbiology* **13**, 2342–2350 (2011).
56. Li, J. *et al.* Intracellular silicification by early-branching magnetotactic bacteria. *Sci. Adv.* **8**, eabn6045 (2022).
57. Li, J. *et al.* Crystal growth of bullet-shaped magnetite in magnetotactic bacteria of the *Nitrospirae* phylum. *J. R. Soc. Interface.* **12**, 20141288 (2015).
58. Lin, W. *et al.* Genomic insights into the uncultured genus ‘Candidatus Magnetobacterium’ in the phylum Nitrospirae. *ISME J* **8**, 2463–2477 (2014).
59. Spring, S. *et al.* Dominating Role of an Unusual Magnetotactic Bacterium in the Microaerobic Zone of a Freshwater Sediment. *Appl Environ Microbiol* **59**, 2397–2403 (1993).
60. Kolinko, S., Richter, M., Glöckner, F.-O., Brachmann, A. & Schüler, D. Single-cell genomics of uncultivated deep-branching magnetotactic bacteria reveals a conserved set of magnetosome genes. *Environmental Microbiology* **18**, 21–37 (2016).
61. Uzun, M. *et al.* Detection of interphylum transfers of the magnetosome gene cluster in magnetotactic bacteria. *Front. Microbiol.* **13**, 945734 (2022).

62. Zhao, Y. *et al.* Insight into the metabolic potential and ecological function of a novel Magnetotactic Nitrospirota in coral reef habitat. *Front. Microbiol.* **14**, 1182330 (2023).
63. Kolinko, S. *et al.* Single-cell analysis reveals a novel uncultivated magnetotactic bacterium within the candidate division OP3. *Environmental Microbiology* **14**, 1709–1721 (2012).
64. Rahn-Lee, L. *et al.* A Genetic Strategy for Probing the Functional Diversity of Magnetosome Formation. *PLoS Genet* **11**, e1004811 (2015).
65. Grant, C. R., Rahn-lee, L. & Legault, K. N. Genome Editing Method for the Anaerobic Magnetotactic. *Applied and Environmental Microbiology* **84**, 1–12 (2018).